Engineering Analysis with Boundary Elements 186 (2026) 106688

Contents lists available at ScienceDirect

Engineering Analysis with Boundary Elements

journal homepage: www.elsevier.com/locate/enganabound

Periodicity thresholds and optimal control in a negative chemotaxis system with cell death

Federico Herrero-Hervás [a,b,c,*], Mihaela Negreanu [a], Antonio M. Vargas [d]

[a] Instituto de Matemática Interdisciplinar, Departamento de Análisis Matemático y Matemática Aplicada, Universidad Complutense de Madrid, Madrid, 28040, Spain
[b] Universität Paderborn, Paderborn, 33098, Germany
[c] Departamento de Matemática Aplicada, ICAI, Universidad Pontificia de Comillas, Madrid, 28015, Spain
[d] Departamento de Matemática Aplicada I, ETSI Industriales, UNED, Madrid, 28040, Spain

ARTICLE INFO

Keywords:
Chemotaxis
Periodicity
Meshless methods
Generalized finite difference method
Optimal control

ABSTRACT

We numerically investigate a nonlinear system of parabolic partial differential equations modeling the negative chemotaxis interactions between a biological species and a lethal chemical substance that is externally supplied. The work extends the knowledge regarding the solutions to an ODE system to which the solutions of the original PDE model converge, as well as the regime of this convergence beyond the existing analytical results.

In particular, for a periodic supply of the substance, a threshold value for the periodicity of the solutions to the ODE system is determined through systematic numerical experiments. Under the obtained conditions – weaker than the current analytical characterization – the convergence and eventual periodicity of the solutions to the PDE model is verified by meshless numerical simulations using the Generalized Finite Difference (GFD) method.

Lastly, an optimal control problem is considered, and an approximate solution is constructed. A Forward-Backward Sweep algorithm combined with the GFD resolution provides the approximate optimal states.

1. Introduction

Chemotaxis is a biological phenomenon through which organisms can detect gradients of a chemical substance and orient their movements towards or against them. If the substance is beneficial for the biological species – for instance a nutrient – the attraction of individuals towards the regions of greater concentration is called *positive* chemotaxis, while for harmful chemicals – such as poisons or antibiotics – the process of repulsion is known as *negative* chemotaxis.

Throughout this paper, we numerically investigate different properties of a model for the negative chemotactic response of a species to a lethal substance, which in non-dimensional form is given by

$$\begin{cases} \dfrac{\partial u}{\partial t} = D\Delta u + \chi\nabla\cdot(u\nabla v) + ru(1-u) - uv, & \boldsymbol{x}\in\Omega,\ t>0,\\ \dfrac{\partial v}{\partial t} = \Delta v + au - v + f(\boldsymbol{x},t), & \boldsymbol{x}\in\Omega,\ t>0, \end{cases} \tag{1}$$

where $u(\boldsymbol{x},t)$ represents the population density of the species, and $v(\boldsymbol{x},t)$ the concentration of the substance, for $\boldsymbol{x}\in\Omega$, $t>0$. The system, introduced in [1], accounts for the following interactions.

(i) For the species: cell diffusion, negative chemotaxis against the gradients of the substance, logistic growth, and the lethal effect of the substance.
(ii) For the substance: diffusion, degradation (in the form of a time decay), self-production by the individuals of the species, and an external supply.

System (1) is completed with nonnegative initial values and Neumann homogeneous boundary conditions

$$\begin{cases} u(\boldsymbol{x},0)=u_0(\boldsymbol{x})\geq 0, \quad v(\boldsymbol{x},0)=v_0(\boldsymbol{x})\geq 0, & \boldsymbol{x}\in\Omega,\\ \dfrac{\partial u}{\partial \nu}=\dfrac{\partial v}{\partial \nu}=0, & \boldsymbol{x}\in\partial\Omega,\ t>0, \end{cases} \tag{2}$$

posed over a bounded domain $\Omega\subset\mathbb{R}^n$ with smooth boundary, with parameters D, χ, $r>0$, $a\geq 0$ respectively representing the diffusion coefficient of the species, the negative chemotactic sensitivity, the logistic growth rate, and the (possibly zero) self-production rate of the substance by the individuals. The source term $f(\boldsymbol{x},t)$, which is assumed

* Corresponding author at: Instituto de Matemática Interdisciplinar, Departamento de Análisis Matemático y Matemática Aplicada, Universidad Complutense de Madrid, Madrid, 28040, Spain.
E-mail address: fedher01@ucm.es (F. Herrero-Hervás).

https://doi.org/10.1016/j.enganabound.2026.106688
Received 17 December 2025; Received in revised form 23 January 2026; Accepted 12 February 2026

to be nonnegative, represents a known external supply of the substance, and ν denotes the outward unit normal vector to the boundary $\partial\Omega$.

Such interactions appear in various biological systems. For instance, it is known that *E. coli* bacteria exhibit negative chemotaxis towards H_2O_2 [2], a substance that is not only lethal for them [3], but also self-produced by the individuals as a metabolic by-product [4,5]. The parameter a also accounts for the case $a = 0$, which results in systems where the substance is not self-produced by the individuals. This broadens the applicability of system (1) to other cases, such as the interactions of bacteria with exogenous antibiotics (those that are not secreted by the species itself).

From a mathematical point of view, system (1) arises as an extension to the classical Keller–Segel system, the first model developed for chemotaxis, introduced in [6,7]. Over the years, a significant body of research has been developed for its numerous variants, as can be seen in the surveys [8–10].

For our particular system (1), different analytical properties have been studied, especially concerning the asymptotic behavior of its solutions. Mainly, the dynamics of the system are driven by two different opposing processes. On the one hand, the negative taxis forces individuals to move away from the areas of larger concentration of the substance. However, if $a > 0$, the self-production of the substance results in an increase of v in those areas where u is greater. This can eventually produce further repulsion if the concentration of the substance becomes too large. On the other hand, the logistic growth of u can be counterbalanced by the external supply of v, depending on the relative size of f. In particular, if f is sufficiently large, the proliferation of the species can be prevented, thereby avoiding its spread.

At the moment, such properties have only been analyzed if the external supply $f(\boldsymbol{x},t)$ is either constant [1] or asymptotically only time-dependent [11], meaning that $f(\boldsymbol{x},t) \to \tilde{f}(t)$, for a certain time-dependent $\tilde{f}(t)$, in a certain sense specified in Section 2. Particularly, in this last case, if r satisfies certain largeness hypothesis, it is known that (u,v), the solution to system (1) with initial and boundary conditions (2), converges to $(\tilde{u},\tilde{v})$, the corresponding solution to the associated ODE system

$$\begin{cases} \dfrac{d\tilde{u}}{dt} = r\tilde{u}(1-\tilde{u}) - \tilde{u}\tilde{v}, & t > 0, \\ \dfrac{d\tilde{v}}{dt} = a\tilde{u} - \tilde{v} + \tilde{f}, & t > 0, \end{cases} \tag{3}$$

with initial values

$$\tilde{u}(0) = \frac{1}{|\Omega|}\int_\Omega u_0(\boldsymbol{x})\,d\boldsymbol{x}, \quad \tilde{v}(0) = \frac{1}{|\Omega|}\int_\Omega v_0(\boldsymbol{x})\,d\boldsymbol{x}. \tag{4}$$

Thus, under those hypotheses, the long-time dynamics of the solutions to the full PDE system (1) are determined by those of the associated ODE system (3). However, the asymptotic behavior of such solutions $(\tilde{u},\tilde{v})$ is not completely understood. An important unresolved case arises if $\tilde{f}$ is a time-periodic function of period $T > 0$, where it is yet not clear under which conditions $(\tilde{u},\tilde{v})$ inherit the periodicity of $\tilde{f}$.

In the particular case $a = 0$, system (3) is uncoupled, and an exact threshold $r_{\min}$ can be determined characterizing the periodicity of its solutions. Precisely, if $r > r_{\min}$, the system admits a unique positive periodic solution, to which any other solution starting from nonnegative initial values converges. Conversely, if $r \le r_{\min}$ no such solution exists, and $\tilde{u}(t) \to 0$ as $t \to \infty$. For this case $a = 0$, this precise threshold $r_{\min}$ coincides with the sufficient largeness hypothesis for r ensuring the convergence of (u,v) to $(\tilde{u},\tilde{v})$, and thus $r_{\min}$ also characterizes the periodicity of the full PDE system (1).

The analysis for the case $a > 0$ is however much more involved due to the nonlinear coupling. In particular, no sharp threshold has been found that characterizes the periodicity of the solutions, only the sufficient condition that guarantees that (u,v) converge to $(\tilde{u},\tilde{v})$.

Main results and structure of the paper

Given the lack of sharp analytical characterizations for the case $a > 0$, this paper aims at numerically exploring its possible threshold conditions, as well as the convergence of (u,v) to $(\tilde{u},\tilde{v})$ in the parameter regimes for which no analytical result has been obtained at the moment.

In particular after the preliminaries in Section 2, a detailed numerical investigation of the properties of system (3) is carried out in Section 3. Starting with the benchmark case $a = 0$, a moving-average method is developed to check the asymptotic periodicity of solutions under different parameter configurations. A systematic approach is followed in order to characterize the results for $a > 0$. Our results consistently suggest that the same threshold $r_{\min}$ is extended, independently of the value of $a > 0$.

Next, with the aim of validating the convergence of (u,v) to $(\tilde{u},\tilde{v})$ and its eventual periodicity in the unknown regimes, various numerical simulations of system (1) are performed. To do so, we employ the Generalized Finite Difference (GFD) method, a meshless numerical approach that has already been successfully used for the resolution of different chemotaxis-type systems (see for instance [12–14]). In Section 4, the preliminaries of the method are included for completeness, and an explicit scheme is presented along with a corresponding bound for the time step to ensure its convergence. The method is tested on irregular distributions of nodes, and used to compute numerical resolutions of system (1) in Section 5, validating the previous conclusions derived from the ODE system regarding the convergence and periodicity.

Lastly, motivated by the results obtained, which allow us to extend the convergence of (u,v) to $(\tilde{u},\tilde{v})$ to cases that have not been characterized analytically – particularly to those in which $\tilde{u}(t) \to 0$ –, in Section 6 we formulate an optimal control problem for system (1). Considering the external supply of substance $f(\boldsymbol{x},t)$ as the control, we define a functional to minimize with the aim of preventing the proliferation of the species. Given the convergence to the solution to the associated ODE system (3), we approximate the original problem by its ODE counterpart, which for the analysis is considerably simpler. After a numerical resolution of the ODE optimal control problem by means of the Forward-Backward Sweep method, we test the obtained control on the full PDE system through another numerical resolution, again through the GFD method.

2. Some preliminaries on the system

Different analytical properties of system (1) posed over a smooth convex bounded domain $\Omega \subset \mathbb{R}^n$ have recently been studied. For a general bounded source $f \in L^\infty(\Omega\times(0,\infty)) \cap C^1(\Omega\times(0,\infty))$, it is known that if r is sufficiently large, system (1) with nonnegative initial values $u_0 \in C^0(\bar{\Omega})$, $v_0 \in W^{1,\theta}(\Omega)$ for some $\theta > n$ and boundary conditions (2) admits a globally defined classical solution (u,v), bounded in $L^\infty(\Omega\times(0,\infty))$ [11]. However, its behavior strongly depends on the choice of f.

If f is constant, the linearized dynamics of the system depend on the ratio between r, the logistic growth rate, and the constant value of f. In particular, two different regimes arise:

1. If $f > r$, there exists a unique non-negative spatially homogeneous steady state, given by $(0,f)$, which is locally asymptotically stable. From a biological point of view, as the supply rate exceeds the species reproductive rate, any solution with initial values close to $(0,f)$ will – at least locally in time – remain close to it, preventing the proliferation of the species.
2. If $f < r$, a secondary spatially homogeneous steady state appears, given by

$$(u_*, v_*) := \left(\frac{r-f}{r+a}, \frac{r(f+a)}{r+a}\right), \tag{5}$$

which is locally asymptotically stable. In turn, the previous equilibrium $(0, f)$ is now unstable. In this regime, the species can persist despite the presence of the lethal substance, as the growth rate r dominates the supply effect.

Whether these local properties hold globally in time depends on a more specific parameter threshold, as proven in [15]. For the first regime, with $f > r$, if moreover $r > a$, then it is shown that for any choice of (u_0, v_0) satisfying the existence requirements, then

$$\|u\|_{L^2(\Omega)} + \|v - f\|_{L^2(\Omega)} \to 0, \quad \text{as } t \to \infty,$$

confirming that indeed the supply rate of the substance is high enough to control the proliferation of the species.

For the second regime, when $f < r$, if parameters fulfill

$$r > \frac{\chi^4 a^4 u_*^2 + 16 D^2 a^2 - 8 D \chi^2 a^3 u_*}{16 D \chi^2 a^2 u_*^2}, \tag{6}$$

then a similar result can be obtained, having that if $(u_0, v_0) \neq (0, f)$, then

$$\|u - u_*\|_{L^2(\Omega)} + \|v - v_*\|_{L^2(\Omega)} \to 0, \quad \text{as } t \to \infty.$$

If the parameter set does not satisfy (6), for instance if χ is large enough – resulting in a chemotaxis-driven process – then spatially heterogeneous patterns can arise, with the population being divided into clusters of high densities and leaving the remaining parts of the domain almost empty. Several numerical experiments have been carried over in [1] to validate these findings.

When f is not constant, the dynamics of system (1) no longer admit stationary equilibria as in the previous cases. The only existing analytical results concerning the behavior of these solutions correspond to sources $f(\boldsymbol{x}, t)$ with a persisting temporal dependence and a decay in their spatial variation. In particular, in [11] the system is investigated under the hypothesis that $f(\boldsymbol{x}, t) \in L^\infty(\Omega \times (0, \infty)) \cap C^1(\Omega \times (0, \infty))$ converges to a spatially homogeneous function $\tilde{f}(t)$, in the following sense

$$\int_0^\infty \|f - \tilde{f}\|_{L^1(\Omega)}\, dt + \int_0^\infty \|f - \tilde{f}\|^2_{L^2(\Omega)}\, dt + \int_0^\infty \left\| \int_\Omega f - \tilde{f} \right\|^2_{L^2(\Omega)} dt < \infty. \tag{7}$$

This accounts for functions f given for instance by

$$f(\boldsymbol{x}, t) = \tilde{f}(t) + p(t) q(\boldsymbol{x}),$$

where $\tilde{f} \in L^\infty(0, \infty) \cap C^1(0, \infty)$ represents the temporally persistent supply, $q \in L^1(\Omega) \cap L^\infty(\Omega) \cap C^1(\Omega)$ encapsulates the spatial heterogeneities, and $p \in L^1(0, \infty) \cap L^\infty(0, \infty) \cap C^1(0, \infty)$ represents the time decay of such heterogeneities.

As a technical remark, observe that the quantity $\int_\Omega f(\boldsymbol{x}, t)\, dx - \tilde{f}(t)$ is spatially independent, and therefore its $L^2(\Omega)$ norm reduces to

$$\left\| \int_\Omega f - \tilde{f} \right\|_{L^2(\Omega)} = \left| \int_\Omega f - \tilde{f} \right| \cdot |\Omega|^{1/2}.$$

By considering the associated ODE system (3), given by

$$\begin{cases} \dfrac{d\tilde{u}}{dt} = r\tilde{u}(1 - \tilde{u}) - \tilde{u}\tilde{v}, & t > 0, \\ \dfrac{d\tilde{v}}{dt} = a\tilde{u} - \tilde{v} + \tilde{f}(t), & t > 0. \end{cases}$$

with initial values

$$\tilde{u}(0) = \frac{1}{|\Omega|} \int_\Omega u_0(\boldsymbol{x})\, d\boldsymbol{x}, \quad \tilde{v}(0) = \frac{1}{|\Omega|} \int_\Omega v_0(\boldsymbol{x})\, d\boldsymbol{x}, \tag{8}$$

under hypotheses (7) if moreover $r > r_{\min,a}$, given by

$$r_{\min,a} := \max\left\{ \tilde{v}(0),\ a \cdot \max\{\tilde{u}(0), 1\} + \|\tilde{f}\|_{L^\infty(0,\infty)} \right\}, \tag{9}$$

(and an additional further technical requirement on r) it is proven that

$$\|u - \tilde{u}\|_{L^2(\Omega)} + \|v - \tilde{v}\|_{L^2(\Omega)} \to 0, \quad \text{as } t \to \infty, \tag{10}$$

where $(\tilde{u}, \tilde{v})$ is the unique solution to system (3) with initial values (8). Thus, the long-time behavior of the full PDE system (1) is governed by that of the associated ODE system (3).

The role of $r_{\min,a}$ in the proof of the convergence to $(\tilde{u}, \tilde{v})$ lies in the fact that for any $a > 0$, if $r > r_{\min,a}$, then there exists $c > 0$ such that $\tilde{u}(t) > c$ for all $t > 0$, avoiding solutions that decay in time. This is used to obtain some estimates of $1/\tilde{u}$, needed for the convergence. In the particular case $a = 0$, system (3) is uncoupled, and a sharper threshold can be obtained, given by

$$r_{\min} := \frac{1}{T} \int_0^T \tilde{f}(s)\, ds, \tag{11}$$

where we recall that T is the period of $\tilde{f}(t)$. Without a strictly positive lower bound for $\tilde{u}$, no long-time analysis is currently available. This means that the possible extinction of the population under time-dependent supplies of the substance is not characterized by the known results, limiting the analysis to small enough supplies, as $r_{\min,a}$ in (9) depends on $\|\tilde{f}\|_{L^\infty(0,\infty)}$.

Closely connected to this, one of the most interesting cases corresponds to a time-periodic $\tilde{f}$. In this setting, the natural question that arises is under which conditions do solutions $(\tilde{u}, \tilde{v})$ inherit the temporal periodicity of $\tilde{f}$. For the simplest case, corresponding to $a = 0$, it is precisely the value of $r_{\min}$ in (11) that acts as a threshold for the periodicity. It is proven in [1] that if $r > r_{\min}$, then the uncoupled version of system (3) admits a unique positive periodic solution, obtained through the pair of initial values $(\tilde{u}(0), \tilde{v}(0)) = (u_0^{per}, v_0^{per})$, given by

$$u_0^{per}(r) := \frac{e^{\int_0^T (r - \tilde{f}(s))\, ds} - 1}{\displaystyle\int_0^T \left(r\, e^{\int_0^s (r - \tilde{f}(\tau))\, d\tau} \right) ds}, \qquad v_0^{per}(r) := \frac{1}{e^T - 1} \int_0^T \tilde{f}(s) e^s\, ds. \tag{12}$$

For any $r > r_{\min}$, a unique pair of initial values (u_0^{per}, v_0^{per}) can be determined by (12), such that the corresponding solution to system (3) is positive and periodic of period T. Moreover, given any other nonnegative pair of initial values, the associated solution converges to the periodic orbit determined by (u_0^{per}, v_0^{per}). Conversely, if $r \leq r_{\min}$, for any nonnegative pair of initial values, the $\tilde{u}$ component of the solution decays to zero, while $\tilde{v}$ preserves the periodic behavior.

For $a > 0$, the question remains open. The threshold $r_{\min,a}$ defined in (9) only guarantees the existence of a positive lower bound for $\tilde{u}$, ruling out any possible decay of to zero. However, this does not directly imply that $(\tilde{u}, \tilde{v})$ is T-periodic. Furthermore, as previously mentioned, $r_{\min,a}$ is not a sharp threshold in the sense of the decoupled case, since substituting $a = 0$ in $r_{\min,a}$ produces a larger value than the exact threshold $r_{\min}$ obtained for $a = 0$. Lastly, if $r \leq r_{\min,a}$ (or $r \leq r_{\min}$ in the case $a = 0$), the lack of a global lower bound for $\tilde{u}$ prevents us from proving the convergence of the solution (u, v) of the full PDE system (1) to $(\tilde{u}, \tilde{v})$, the solution to the ODE system (3).

Thus, we begin our study with the numerical determination of the periodicity threshold, with the purpose of expanding the existing knowledge regarding the asymptotic behavior of the solutions in regimes not covered by the currently available analytical results.

3. Numerical determination of the periodicity threshold

With the aim of exploring the periodic regime in system (3) – even when the convergence of (u, v) to $(\tilde{u}, \tilde{v})$ is not guaranteed –, we numerically integrate the system for different parameter configurations. In order to distinguish between solutions that are asymptotically periodic (i.e. those that converge to a periodic solution) and those that decay, a moving average of the solution is computed over intervals

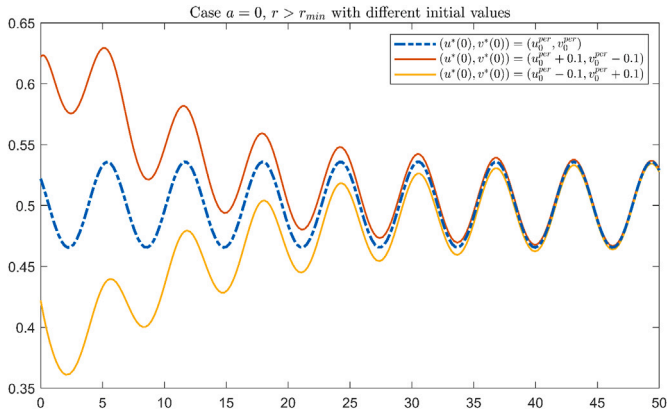

Fig. 1. Numerical resolution of the ODE system (3) with $a = 0$ and $r = 0.2$ for different initial values. Only the $\tilde{u}$ component is shown.

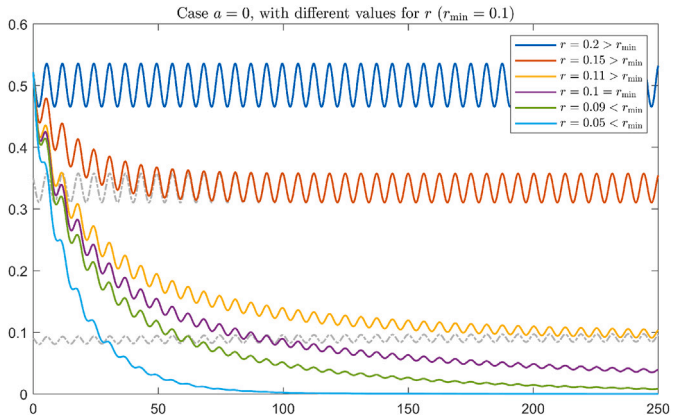

Fig. 2. Numerical resolution of the ODE system (3) with $a = 0$ and different values of r above and below $r_{\min}$, all with the same initial value. The gray curves are the only periodic solutions for $r = 0.15$ and $r = 0.11$, to which the other solutions converge. Only the $\tilde{u}$ component is shown.

corresponding to integer multiples of the period T of $\tilde{f}$, as detailed below.

We begin with the uncoupled case $a = 0$ as a benchmark, for which we know that the periodicity is characterized by the known threshold $r_{\min} = \frac{1}{T}\int_0^T \tilde{f}(s)\, ds$.

3.1. Case $a = 0$

Starting with the uncoupled case $a = 0$, we take a sample source function, given for instance by $\tilde{f}(t) = 0.1 \cdot \big(1 + \cos(t)\big)$, with period $T = 2\pi$. By using (11), we obtain the threshold value

$$r_{\min} = 0.1,$$

which determines the two different possible behaviors of the system.

To begin the numerical study, as a reference value, we take for instance $r = 0.2 > r_{\min}$, with which we have $(u_0^{per}(r), v_0^{per}(r)) \approx (0.522, 0.15)$. To study the dynamics of system (3), we perform a numerical integration, first with initial values $(u_0^{per}(r), v_0^{per}(r))$, and secondly with small perturbations of the former, in this case $(u_0^{per} + \varepsilon, v_0^{per} - \varepsilon)$ and $(u_0^{per} - \varepsilon, v_0^{per} + \varepsilon)$, for $\varepsilon = 0.1$. The results are depicted in Fig. 1, only showing the $\tilde{u}$ component of the solution until $t = 50$. The periodic curve is represented in a blue dashed line, while the other two solutions are plotted in red and yellow. We see how the solutions corresponding to the perturbed initial values converge in time to the periodic solution, as expected by the known explicit solution of the system.

Next, we keep the previous initial value $(\tilde{u}(0), \tilde{v}(0)) = (u_0^{per}(0.2), v_0^{per}(0.2)) \approx (0.522, 0.15)$, corresponding to $r = 0.2$, and test different other values of r below and above $r_{\min}$. In particular, we solve the equations for $r \in \{0.15,\ 0.11,\ 0.1,\ 0.09,\ 0.05\}$, as well as the previous case $r = 0.2$ for reference. The results are plotted in Fig. 2, again only showing the $\tilde{u}$ component, this time until $t = 150$ for better visualization.

As can be seen, the first case directly produces the periodic solution, the same as in Fig. 1, while as expected for $r = 0.15$ and $r = 0.11$, both above $r_{\min}$, the solution ends up converging to the associated periodic solution to such values of r, which is represented in gray dotted line for each case. For $r \le r_{\min}$ no solution with such properties exists, and we see how all three curves seem to decay to zero.

With respect to the $\tilde{v}$ component, as for this case the system is uncoupled, the value of r does not affect its dynamics, which are independent of $\tilde{u}$. Thus, all of the above cases produce the same periodic $\tilde{v}$, as the second component of the initial value v_0^{per} is also independent of r.

With the aim of expanding the analysis to the coupled case with $a > 0$, a computational criterion is needed to distinguish between solutions that slowly converge to a periodic orbit, and those that have a true time decay.

Numerical criterion for periodicity assessment:

Motivated by the previous example, in order to develop a numerical criterion that allows us to distinguish between solutions that are asymptotically periodic and those that decay, we consider a moving average approach. For given values of $r > 0$ and $a \ge 0$, since the external source $\tilde{f}(t)$ is T-periodic, and any periodic asymptotic regime must also inherit the period T, we integrate system (3) over a sufficiently long interval of the form $[0, N \cdot T]$, with a large $N > 0$. With the obtained solution, window averages of $\tilde{u}(t)$ are computed over intervals of the form $[m \cdot T, (m + k) \cdot T]$, for a fixed window length $k \ge 1$ and integers $m \in \{0, \dots, N - k\}$. Denoting these averages by A_m, we analyze the sequence $\{\ln A_m\}_m$.

A strictly decreasing trend in $\ln A_m$ indicates exponential decay of the solution, whereas stabilization of the sequence leads to the convergence toward a nontrivial T-periodic solution. This provides a robust and easily implementable criterion for detecting the periodicity threshold in $r > 0$ for a given $a \ge 0$.

To test the method with the well-studied case $a = 0$, based on the previous choices of $\tilde{f}$ and the results shown in Fig. 2, we consider $r \in \{0.2,\ 0.11,\ 0.09,\ 0.05\}$. For the first two cases, the solution starting at any initial value must be asymptotically periodic, while the last two produce a time decay. As a sample initial value, we take the previous $(u_0^{per}(0.2), v_0^{per}(0.2)) \approx (0.522, 0.15)$, corresponding to the periodic solution for $r = 0.2$. We simulate the system over $N = 250$ periods, that is, in the interval $[0, 500\pi]$, and consider a window length of $k = 10$. The results are represented in Fig. 3, with two different scales on each panel.

As expected, the blue and red curves, corresponding to values of $r > r_{\min}$ soon stabilize, indicating the convergence to a periodic solution. In particular, as the right panel shows, for $r = 0.2$, represented in blue, the sequence is constant, as the initial value was $(u_0^{per}(0.2), v_0^{per}(0.2))$, and thus we directly obtain the periodic solution. The red curve, corresponding to $r = 0.11$ exhibits an initial decay, which had already been observed in the results from Fig. 2, before completely stabilizing after approximately 50 periods.

In contrast, the yellow and purple curves decrease with a seemingly constant slope, indicating an exponential decay, as for these cases $r \le r_{\min}$, and thus the logistic growth rate is too weak to compensate for the external supply, leading to the population decay and eventual extinction.

Having tested the criterion with the benchmark case $a = 0$, we next proceed with the analysis for the coupled case $a > 0$. As a final

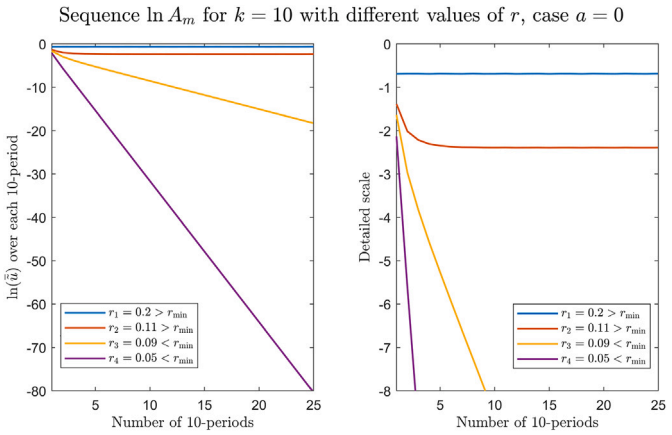

Fig. 3. Sequence $\ln A_m$: mean of $\tilde{u}$ computed over successive 10-period intervals, for $a = 0$ and different values of r. The left panel shows all cases in a full scale while the right panel has a detailed scale to show the stabilization of the first two cases.

remark, once the values of the sequence $\{\ln A_m\}_m$ have been computed, its decrease or stabilization can be numerically checked by using a linear least–squares fit of the values of $\ln A_m$ with respect to m. A slope close to zero indicates that the averages A_m stabilize, while a strictly negative slope corresponds to an exponential decay of the solution. In practice, we classify a trajectory as asymptotically periodic whenever the least-squares slope s is such that $|s| < \varepsilon$ for a small tolerance $\varepsilon > 0$, and as decaying otherwise. This purely numerical criterion is simple to implement and sufficiently robust for the long-time simulations considered in this work.

3.2. Case $a > 0$

Next, we explore the differences with respect to a nonzero choice of a. As a starting point, we consider the same choice of $\tilde{f}$ as in the previous case, given by $\tilde{f}(t) = 0.1 \cdot (1 + \cos(t))$, and we keep r fixed at $r = 0.2 > r_{\min} = 0.1$, the value for $a = 0$.

To analyze the effect of an increasing $a > 0$, we solve the complete system (3) numerically with different choices of a and initial value $(\tilde{u}(0), \tilde{v}(0)) = (u_0^{per}(0.2), v_0^{per}(0.2)) \approx (0.522, 0.15)$, to analyze how the solution diverges from the periodic one for $a = 0$.

We first consider small values of a, in particular $a \in \{0.005,\ 0.01,\ 0.05,\ 0.1\}$ and compute $r_{\min,a}$ as given in (9). As for this example $\tilde{u}(0) < 1$ and $\tilde{v}(0) < \|\tilde{f}\|_{L^\infty(0,\infty)} = 0.2$, we directly have

$$0.2 = r \not> r_{\min,a} = a + \|\tilde{f}\|_{L^\infty(0,\infty)} = a + 0.2,$$

and thus no value of $a > 0$ satisfies the sufficient (but not necessary) criterion to ensure that $\tilde{u}$ remains bounded from below by a positive constant for all $t > 0$. However, as it can be seen in Fig. 4, all considered values of $a > 0$ seem to produce solutions that are asymptotically periodic, approaching a periodic orbit with the same period as $\tilde{f}$. As a reference value, we also plot the periodic solution for $a = 0$. Again, the graph only represents the $\tilde{u}$ component. We also included delimiters for the cases $a = 0.05$ and $a = 1$ in dashed gray lines to visually check their asymptotic periodicity.

The $\tilde{v}$ components are plotted in Fig. 5, this time producing different curves as the equation for $\tilde{v}$ is no longer uncoupled for $a > 0$. For better visibility, we only plot the solution for $t \in [0, 25]$.

As can be directly inferred from the system, increasing the value of a – which represents the rate of self-production of the chemical by the bacteria – leads to higher overall chemical concentrations. Furthermore, for a fixed bacterial density $\tilde{u}$, a higher concentration of the chemical amplifies the death term $-\tilde{u}\tilde{v}$, producing the initial

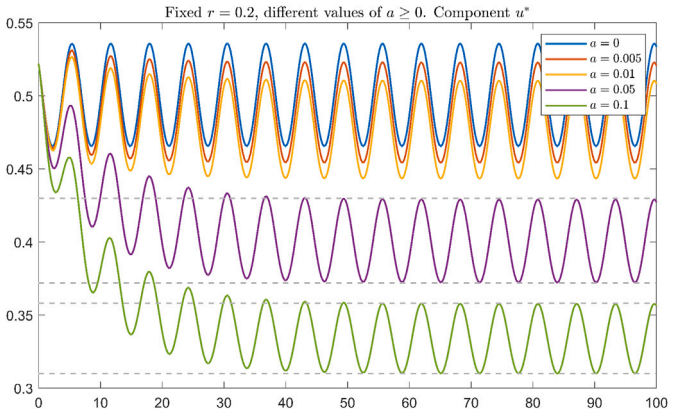

Fig. 4. Numerical resolution of the ODE system (3) with different small values of $a \geq 0$ and fixed $r = 0.2$, all with the same initial value. Only the $\tilde{u}$ component is shown.

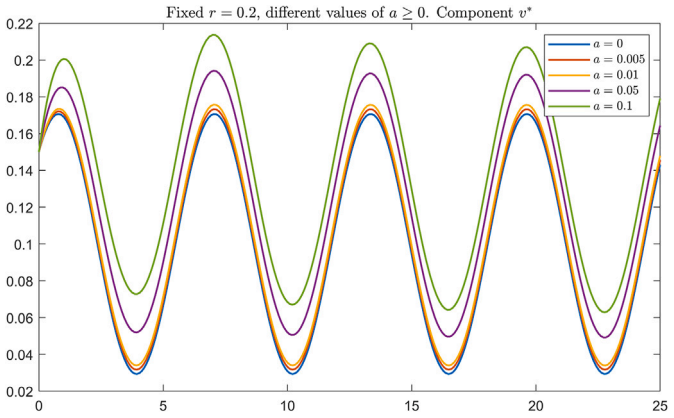

Fig. 5. Component $\tilde{v}$ of the numerical resolution of the ODE system (3) with the parameter values shown in Fig. 4.

decrease observed in Fig. 4 and ultimately yielding lower bacterial densities for larger values of a.

The influence of these changes in a is more visible in the $\tilde{u}$ component than in $\tilde{v}$. This scaling difference arises because the coupled term in the first equation is given by $-\tilde{u}\tilde{v}$, whereas in the second it is $a\tilde{u}$, with the chosen values of a being relatively small. Consequently, variations among the solution curves are more noticeable in $\tilde{u}$, as shown in Fig. 4, than in $\tilde{v}$, as illustrated in Fig. 5.

For larger values of a, simulations in the time interval $[0, 50]$ are represented in Fig. 6. The case $a = 0$ is also included for reference. Again, the initial values are given by $(\tilde{u}(0), \tilde{v}(0)) = (u_0^{per}(0.2), v_0^{per}(0.2))$ to analyze how different solutions diverge.

As noted in the previous case, a greater value of a results in steeper decay in the initial instants, caused by the increase of the death term $-\tilde{u}\tilde{v}$. However, even in the largest cases ($a = 5$ and $a = 10$), the dynamics of the system seem to converge to a periodic regime, and no extinction is achieved. This can be better visualized in Fig. 7, where both cases are represented for $t \in [5, 70]$. These results indicate that at least for the considered values of a, the choice of $r = 0.2$ is large enough to sustain the population, although at a very low level for the larger cases of a.

It is also observed that in this case, for fixed values of r and $\tilde{f}$, the amplitude of the oscillations in $\tilde{u}$ decreases as a increases. This is due to the fact that, for larger values of a, the self-production term $a\tilde{u}$ becomes the leading term in the dynamics of $\tilde{v}$, rather than $\tilde{f}$. Hence, as a grows larger, and the effect of the periodicity imposed by $\tilde{f}$ is progressively reduced.

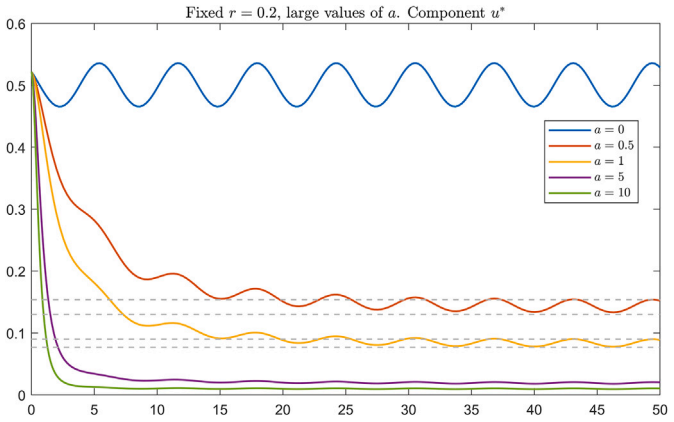

Fig. 6. Numerical resolution of the ODE system (3) with larger values of a for fixed $r = 0.2$. Only the $\tilde{u}$ component is shown.

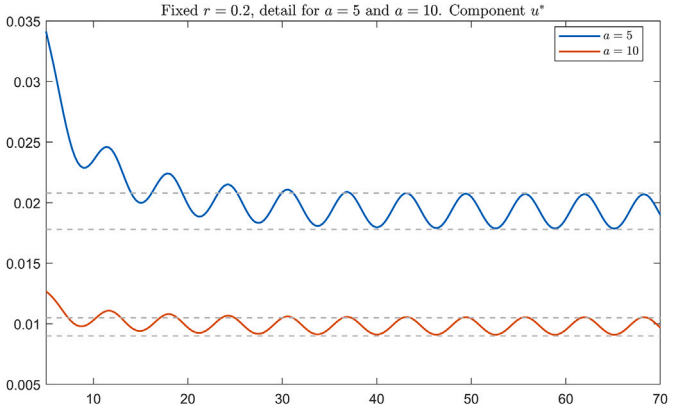

Fig. 7. Detail of Fig. 6 for $a = 5$ and $a = 10$.

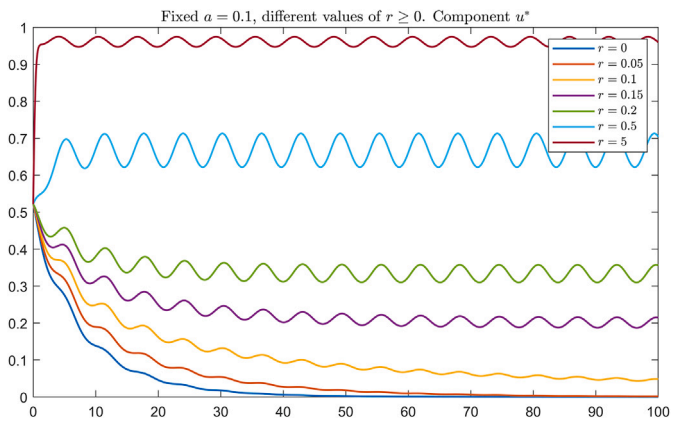

Fig. 8. Numerical resolution of system (3) with $a = 0.1$ and different values of $r \geq 0$. Only the $\tilde{u}$ component is shown.

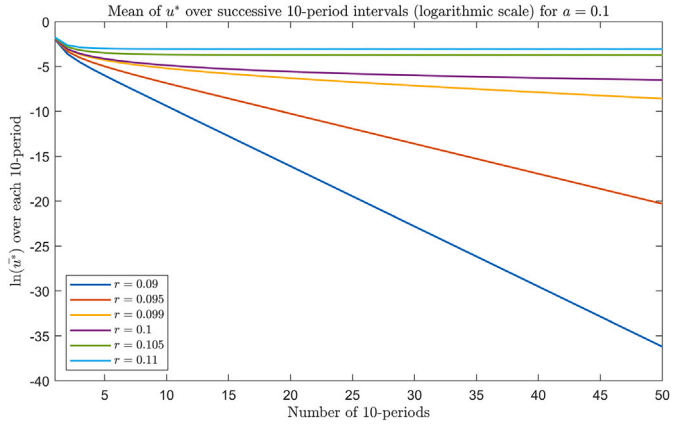

Fig. 9. Mean of $\tilde{u}$ computed over successive 10-period intervals for $a = 0.1$ and different values of r.

Next, we analyze the influence of varying the logistic growth rate r, with the aim of determining the different behaviors of the system to compare them with those obtained for $a = 0$ (decay leading to extinction or periodic persistence depending on $r_{\min}$). In this way, we fix the value of a, first at $a = 0.1$, and consider the same $\tilde{f}$ and $(\tilde{u}(0), \tilde{v}(0))$ as in the previous experiments. To study the possible differences with the case $a = 0$, we take different values of r above and below the previous threshold $r_{\min} = 0.1$. In particular, we consider $r \in \{0,\ 0.05,\ 0.1,\ 0.15,\ 0.2,\ 0.5,\ 1\}$, and solve system (3) numerically. The results are plotted in Fig. 8.

As the image shows, for the cases $r \in \{0,\ 0.05,\ 0.1,\ 0.15,\ 0.2\}$, the solution $\tilde{u}(t)$ exhibits an initial decrease, with the first two cases apparently rapidly decaying to zero. In contrast, for $r \in \{0.5,\ 5\}$ the solution starts increasing at $t = 0$. This qualitative change can be analytically obtained by computing the sign of the initial growth rate of $\tilde{u}$. Indeed, from the first equation in (3), one obtains

$$\frac{d\tilde{u}}{dt}(0) > 0 \quad \text{if and only if} \quad r > \frac{\tilde{u}(0)\,\tilde{v}(0)}{\tilde{u}(0)\big(1 - \tilde{u}(0)\big)}.$$

For the initial data considered, the right-hand side evaluates to 0.3138, which matches the observed results separating the initial growth regimes. This is however only a local phenomenon, as in certain cases (for instance $r = 0.2$), the value of r is large enough to overcome this initial decay and eventually sustain the population in a periodic regime.

To further characterize this transition between decay and periodic persistence observed in Fig. 8 we focus on numerically identifying the corresponding threshold value for r that separates both behaviors, using the window average criterion previously detailed. In particular, given the observed difference between the results obtained for $r = 0.05$ and $r = 0.15$, we consider various values of r close to 0.1 and compute the sequence $\{\ln A_m\}_m$. The results are plotted in Fig. 9.

The results show that for the computed values of r below 0.1, the logarithm of the mean decreases in a linear trend, and thus solutions decay to zero. On the other hand, above $r = 0.1$, for $r = 1.05$ and $r = 0.11$, the stabilization of the mean indicates a convergence towards a periodic curve. These results seem to suggest that – at least for the small choice of a considered for this case – the threshold for a that separates both behaviors might still be at $r_{\min} = 0.1$, the same as for $a = 0$.

To investigate the dependency of this threshold with respect to a, we compute the same mean of $\tilde{u}$ over 500 intervals of length $10 \cdot T$ with two fixed values of r, one below and one above $r_{\min} = 0.1$, considering different values of a. In particular, we select $r_1 = r_{\min} + 0.001 = 0.101$, and $r_2 = r_{\min} - 0.001 = 0.099$, and compute the mean with values of $a \in \{0,\ 0.5,\ 2,\ 10\}$. The value of $a = 0$ is included again as a reference value, to compare with the previous well-understood case. The results are gathered in Fig. 10. Each color represents a fixed value of a, while the solid line corresponds to the computed value with $r = r_1 = 0.101$, and the dashed line with $r = r_2 = 0.099$.

As observed, for all the considered values of a, the solid curves corresponding to $r = r_1$ reach a stable regime, indicating convergence to a periodic orbit, whereas the dashed lines associated to $r = r_2$ continue to decrease over time in a linear fashion, leading to extinction through an exponential decay. In this way, the results seem to indicate that the threshold value of r determining the qualitative behavior of $\tilde{u}$ may in

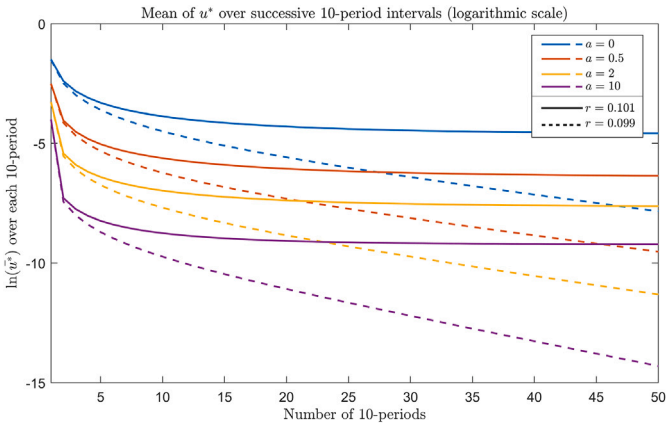

Fig. 10. Mean of $\tilde{u}$ computed in successive 10-period intervals for different values of a, with $r \in \{r_1, r_2\}$.

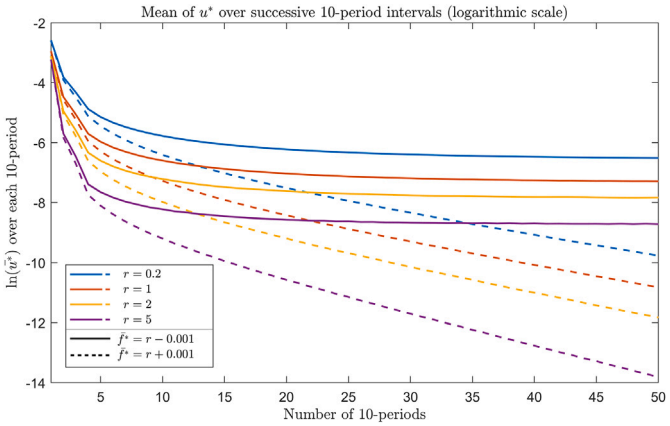

Fig. 11. Mean of $\tilde{u}$ computed in successive 10-period intervals for $a = 0.5$, with $r \in \{0.2,\ 1,\ 2,\ 5\}$, $\tilde{f}$ as in (13), $M = r + 0.001$ and $M = r - 0.001$.

fact be independent of a. Thus, the threshold value for r in the case $a > 0$ might in fact be preserved from the case $a = 0$, as the same value of $r_{\min}$ seems to separate the two possible behaviors of the system.

To evaluate this possibility, we study the role of the external supply in the dynamics of the system, modifying the average value of $\tilde{f}$ to assess the changes in the threshold. To this end, we consider the source function $\tilde{f}$ given by

$$\tilde{f}(t) = M \cdot \big(1 + \cos(t)\big), \tag{13}$$

for $M > 0$, so that for the case $a = 0$, by (11), $r_{\min} = \bar{\tilde{f}} = M$, where $\bar{\tilde{f}}$ represents the average of $\tilde{f}$ over its period. Considering the results of the previous experiments, for our analysis we can only vary r and M and keep $a > 0$ fixed, which in principle does not affect the value of the threshold.

Our aim is to study the relationship between $\bar{\tilde{f}}$, which determines the value of $r_{\min}$ for $a = 0$, and the actual threshold for r in this case $a > 0$. Taking for instance $a = 0.5$, and $r \in \{0.2,\ 1,\ 2,\ 5\}$,we solve system (3) numerically for each of these values of r, with $\tilde{f}$ as in (13), for $M = r + 0.001$ and $M = r - 0.001$. To determine the behavior of the solution $\tilde{u}$, we compute the sequences $\{\ln A_m\}_m$ as in the previous cases. The results are depicted in Fig. 11.

As can be seen in the image, regardless of the value of r, the cases $\bar{\tilde{f}} = r - 0.001$ (for which $r > r_{\min} = \bar{\tilde{f}}$), represented in solid lines, produce a mean that stabilizes with time, leading to a persistent periodicity. In contrast, those with $\bar{\tilde{f}} = r + 0.001$ (for which $r < r_{\min} = \bar{\tilde{f}}$) decay in time, indicating extinction.

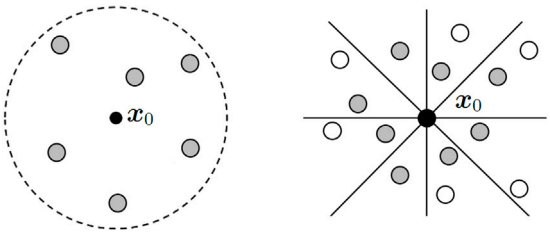

Fig. 12. Left panel: Sketch of a GFD star with $s = 6$ nodes centered on $\boldsymbol{x}_0$. Right panel: $s = 8$ nodes selected by the octant criterion colored in gray.

Therefore, the numerical results consistently seem to indicate that in fact the case $a > 0$ inherits the same threshold for r as the original case $a = 0$, which could be analytically analyzed, yielding the value of $r_{\min}$ in (11). While the dynamics of the full system with $a > 0$ are more intricate due to the nonlinear coupling introduced by the self-production term – as illustrated in Figs. 4 and 5 – the transition between persistence and extinction appears to be governed by the same underlying mechanism as in the uncoupled case, independently of the value of $a > 0$. These conclusions are, however, based solely on numerical evidence and remain to be rigorously proven analytically.

4. Meshless discretization via the generalized finite difference method

Next, having discussed the possible behaviors of the ODE system (3), in this section we present the framework for the Generalized Finite Difference (GFD) Method, which will be used to obtain a numerical scheme to compute the numerical experiments for the full PDE system (1).

4.1. Brief description of the method

The GFD Method arises as a meshless extension of the classical Finite Difference Method, allowing one to solve boundary value problems on general bounded domains with no strong geometric regularity. Originally developed in 1960 by Collatz in [16] and by Forsythe and Wasow in [17], the method was later reintroduced in the 1970s by Jensen [18] and Perrone and Kao [19]. Different improvements have been investigated over the years, as seen for example in [20], and as mentioned in the Introduction, it is widely used for the numerical resolution of chemotaxis-type equations [12–14].

The method requires a set of nodes that can be irregularly distributed over the domain, on which the solution is to be approximated. The numerical scheme is constructed by obtaining finite difference approximation formulae for the partial derivatives appearing in the equation. For clarity, we present the formulation in two spatial dimensions, being easily generalized to higher dimensional problems.

To this end, let $M = \{\boldsymbol{x}_1, \dots, \boldsymbol{x}_N\}$ be the cloud of nodes that constitute the discretization of the domain Ω, and let $\boldsymbol{x}_0$ denote an arbitrary interior node of M. Around $\boldsymbol{x}_0$ we construct a local GFD star, consisting of a fixed number s of neighboring nodes, as shown in the left panel of Fig. 12, which will be used to approximate the partial derivatives at $\boldsymbol{x}_0$. Several strategies may be used to select the neighboring nodes, such as quadrant, octant, or distance-based criteria. The right panel of Fig. 12 represents the 8 nodes selected by the octant criterion introduced in [19], where one node is chosen from each angular sector around $\boldsymbol{x}_0$, typically by distance.

Let $w(\boldsymbol{x}, t)$ denote any of the components (u, v) of the continuous solution we seek to approximate. Given any node $\boldsymbol{x}_i$ within the GFD star, at any fixed $t > 0$, by making use of a second-order Taylor expansion of w centered at $\boldsymbol{x}_0$, one has

$$w(\boldsymbol{x}_i, t) \approx w(\boldsymbol{x}_0, t) + (\boldsymbol{x}_i - \boldsymbol{x}_0) \cdot \nabla w(\boldsymbol{x}_0, t) + \frac{1}{2}(\boldsymbol{x}_i - \boldsymbol{x}_0)^T \cdot H_w(\boldsymbol{x}_0, t) \cdot (\boldsymbol{x}_i - \boldsymbol{x}_0),$$

where H_w denotes the Hessian matrix of w. By denoting as usual by W_i^n the approximation of $w(\boldsymbol{x}_i, t_n)$, a function B can be defined for the s nodes contained in the star, given by

$$B(W_0^n) = \sum_{i=1}^{s} \tilde{w}_i^2 \left[\left(W_0^n + h_i \frac{\partial W_0^n}{\partial x} + k_i \frac{\partial W_0^n}{\partial y} + \frac{1}{2}\left(h_i^2 \frac{\partial^2 W_0^n}{\partial x^2} + k_i^2 \frac{\partial^2 W_0^n}{\partial y^2} + 2h_i k_i \frac{\partial^2 W_0^n}{\partial x \partial y} \right) \right) - W_i^n \right]^2, \tag{14}$$

where (h_i, k_i) denote the x and y coordinates of $(\boldsymbol{x}_i - \boldsymbol{x}_0)$, respectively, and $\tilde{w}_i$ are weights that decrease with the distance from $\boldsymbol{x}_0$ to $\boldsymbol{x}_i$, taken for instance as $\tilde{w}_i = (h_i^2 + k_i^2)^{-\alpha}$ for some $\alpha > 0$ (see [21,22]). In this way, B measures the weighted sum of quadratic errors made when approximating each W_i^n by the above Taylor expansion centered on $\boldsymbol{x}_0$.

Thus, minimizing B with respect to the partial derivatives appearing in the expansion, results in their best second-order least-squares approximation based on the s nodes of the star. This provides finite-difference formulae that can be substituted in the original PDE system to obtain a numerical scheme. In particular, B can be rewritten as

$$B(W_0^n) = \sum_{i=1}^{s} \tilde{w}_i^2 (W_0^n - W_i^n + \mathbf{c}_i^T \cdot \mathbf{d}^n)^2, \tag{15}$$

where

$$\mathbf{c}_i := \left(h_i,\ k_i,\ \frac{h_i^2}{2}, \frac{k_i^2}{2},\ h_i k_i \right)^T,$$

$$\mathbf{d}^n := \left(\frac{\partial W_0^n}{\partial x},\ \frac{\partial W_0^n}{\partial y},\ \frac{\partial^2 W_0^n}{\partial x^2},\ \frac{\partial^2 W_0^n}{\partial y^2},\ \frac{\partial^2 W_0^n}{\partial x \partial y} \right)^T.$$

Since B is quadratic, to minimize it, a direct differentiation with respect to the elements in $\mathbf{d}^n$ results in a linear system of 5 equations, which can be expressed as

$$A \cdot \mathbf{d}^n = \mathbf{b}^n, \tag{16}$$

where the coefficient matrix A and the right-hand side vector $\mathbf{b}^n$ are given by

$$A := \sum_{i=1}^{s} \tilde{w}_i^2 \mathbf{c}_i \mathbf{c}_i^T, \quad \mathbf{b}^n := -\sum_{i=1}^{s} \tilde{w}_i^2 (W_0^n - W_i^n)\mathbf{c}_i. \tag{17}$$

The properties of A are well-known [22]. In particular, by construction, it is symmetric and positive semidefinite. Moreover, A becomes positive definite whenever the star is nondegenerate, that is, in dimension 2, when the vectors $\{\mathbf{c}_i\}_{i=1}^s$ span $\mathbb{R}^5$. In this case, the linear system admits a unique solution, providing the second-order least-squares finite difference formulae for the partial derivatives. The node selection criteria previously mentioned are designed to guarantee a sufficiently rich local geometry around $\boldsymbol{x}_0$, ensuring that the vectors $\{\mathbf{c}_i\}_{i=1}^s$ indeed span $\mathbb{R}^5$, resulting in a nonsingular matrix A. These criteria effectively avoid the common degeneracies associated with nearly collinear or otherwise poorly distributed stars, ensuring the numerical robustness and solvability of the GFD discretization.

We moreover emphasize that A depends only on the geometry of the local star and the chosen weights, and therefore it is independent of time. Consequently, its factorization can be precomputed once and used at all time steps, which yields a substantial reduction in the computational cost of the method.

Lastly, by introducing

$$\mathbf{m}_i := \tilde{w}_i^2 A^{-1} \mathbf{c}_i, \quad \mathbf{m}_0 := \sum_{i=1}^{s} \mathbf{m}_i,$$

and denoting by m_{ij} the jth component of $\mathbf{m}_i$, for $i \in \{1, \dots, s\}$, $j \in \{1, \dots, 5\}$, the second-order least-squares finite difference approximations for the partial derivatives of $w(\boldsymbol{x}_0, t_n)$ can be computed as

$$\begin{cases} \dfrac{\partial w(\boldsymbol{x}_0, t_n)}{\partial x} = -m_{01} W_0^n + \displaystyle\sum_{i=1}^{s} m_{i1} W_i^n + \mathcal{O}(h_i^2, k_i^2), \\ \dfrac{\partial w(\boldsymbol{x}_0, t_n)}{\partial y} = -m_{02} W_0^n + \displaystyle\sum_{i=1}^{s} m_{i2} W_i^n + \mathcal{O}(h_i^2, k_i^2), \\ \dfrac{\partial^2 w(\boldsymbol{x}_0, t_n)}{\partial x^2} + \dfrac{\partial^2 w(\boldsymbol{x}_0, t_n)}{\partial y^2} = -(m_{03} + m_{04}) W_0^n + \displaystyle\sum_{i=1}^{s} (m_{i3} + m_{i4}) W_i^n \\ \qquad\qquad =: -m_{00} W_0 + \displaystyle\sum_{i=1}^{s} m_{i0} W_i + \mathcal{O}(h_i^2, k_i^2). \end{cases} \tag{18}$$

Lastly, to obtain an explicit scheme, a first-order forward difference formula can be employed to discretize the time derivative, this is

$$\frac{\partial w(\boldsymbol{x}_0, t_n)}{\partial t} = \frac{W_0^{n+1} - W_0^n}{t_{n+1} - t_n} + \mathcal{O}(\Delta t). \tag{19}$$

In principle, a constant time step can considered, denoted here by Δt. Substituting the discretizations (18) and (19) in the partial derivatives appearing in system (1) results in an explicit scheme, initialized with the corresponding initial values $u(\boldsymbol{x}, 0)$ and $v(\boldsymbol{x}, 0)$.

For boundary nodes subject to Neumann conditions, one simple and commonly used alternative is to employ first-order finite difference formulae based on neighboring nodes are chosen only inside the domain, aligned with the outward normal direction, which prevents considering one-sided stars. When higher order accuracy is required, artificial nodes can be placed outside the domain so that a non-degenerate star can be obtained near the boundary (see for instance [23]).

4.2. Numerical scheme

Having established the construction of the local GFD stars and the corresponding least-squares approximation of the partial derivatives, we now state the resulting discrete scheme used to approximate the solutions to system (1). The formulation presented here follows the scheme introduced in our previous work [1], included for completeness and to ensure that the numerical analysis in the subsequent sections is fully self-contained.

The scheme, for every inner node, reads as

$$\begin{cases} u_0^{n+1} = u_0^n + \Delta t \left[D\left(-m_{00} u_0^n + \displaystyle\sum_{i=1}^{s} m_{0i} u_i^n \right) - \chi u_0^n \left(-m_{00} v_0^n + \displaystyle\sum_{i=1}^{s} m_{0i} v_i^n \right) \right] \\ \qquad + \chi \Delta t \left(-m_{01} u_0^n + \displaystyle\sum_{i=1}^{s} m_{i1} u_i^n \right) \left(-m_{01} v_0^n + \displaystyle\sum_{i=1}^{s} m_{i1} v_i^n \right) \\ \qquad + \chi \Delta t \left(-m_{02} u_0^n + \displaystyle\sum_{i=1}^{s} m_{i2} u_i^n \right) \left(-m_{02} v_0^n + \displaystyle\sum_{i=1}^{s} m_{i2} v_i^n \right) \\ \qquad + \Delta t \cdot r u_0^n \left(1 - u_0^n \right) - \Delta t u_0^n v_0^n, \\ v_0^{n+1} = v_0^n \left(1 - \Delta t \cdot (1 + m_{00}) \right) + \Delta t \cdot a u_0^n + \Delta t \displaystyle\sum_{i=1}^{s} m_{0i} v_i^n + f_0^n, \end{cases} \tag{20}$$

which is initiated with the initial values $u(\boldsymbol{x}, 0)$ and $v(\boldsymbol{x}, 0)$.

As in standard finite-difference discretizations of parabolic problems, the explicit nature of the method imposes a stability restriction on the time step. In this case, we state the following convergence result developed in [1], where the details of the proof can be consulted.

Theorem 4.1 (*Theorem 5.1 in [1]*). *The GFD explicit scheme (20) is convergent if*

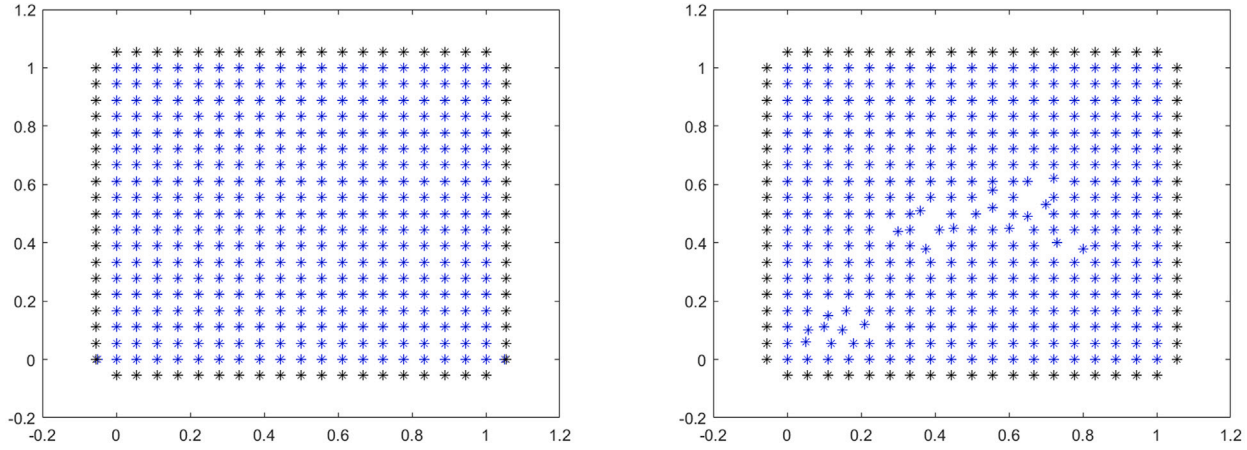

Fig. 13. The two different discretizations of Ω considered.

$$\Delta t < \min\left\{ \frac{2}{m_{00} + \sum_{i=1}^{s} |m_{i0}| + A_1 + B_1}, \frac{2}{1 + m_{00} + \sum_{i=1}^{s} |m_{i0}| + \Delta t \cdot a} \right\}, \tag{21}$$

for every inner node, where A_1 and B_1 are certain coefficients obtained in the proof.

5. Numerical experiments

Once the numerical scheme (20) has been derived in Section 4, we first perform various numerical tests to verify the obtained approximation formulae of the partial derivatives. Next, we carry out several numerical resolutions of system (1) to study the evolving dynamics, both on short timescales, where the spatial effects of diffusion and chemotaxis are more dominant; as well as its long-time behavior. For $r > r_{\min,a}$, the eventual convergence and periodicity properties established in Section 2 will be validated numerically. Moreover, the opposite case with $r \leq r_{\min,a}$ – of special analytical interest due to the lack of asymptotic results –, will also be examined with different examples.

For all numerical experiments, we consider the convex and bounded domain $\Omega = [0,1]\times[0,1]$. Although the geometry of the unit square Ω is particularly suitable for classical Finite Difference (FD) schemes, due to its regular structure, we employ it as a benchmark to assess the results of the GFD method. To this end, two distinct spatial discretizations of Ω are considered, a uniform grid of evenly spaced nodes, well-suited to the classical FD framework; and a nonuniform cloud of points obtained by introducing localized irregularities into the uniform grid, where only the GFD method can be used.

In particular, a total of 437 nodes are considered in both discretizations (evenly spaced in the regular grid, placed within a distance of $1/18$), out of which 76 are fictitious, surrounding the boundary of Ω, to account for the boundary conditions. Both discretizations are shown in Fig. 13, with the irregularities of the second one being clearly visible, with fictitious nodes represented in black.

5.1. Polynomial test for the GFD discretization scheme

Before computing any numerical resolution of system (1), we test the approximation formulae for the partial derivatives provided by the GFD method over the nodes in the irregular discretization of Ω.

In particular, as the scheme was obtained by a truncated second-order Taylor expansion, we consider a basis of quadratic polynomials in two dimensions, given by

$$\mathcal{B} = \{1,\ x,\ y,\ x^2,\ xy,\ y^2\}. \tag{22}$$

By applying the second-order GFD discretization of the spatial partial derivatives of the polynomials in $\mathcal{B}$, the obtained results must reproduce their partial derivatives exactly up to working precision.

For the scheme, we consider stars composed of 8 nodes, selected by the octant criteria. The partial derivatives $\frac{\partial}{\partial x}$, $\frac{\partial}{\partial y}$, $\frac{\partial^2}{\partial x^2}$, $\frac{\partial^2}{\partial y^2}$, $\frac{\partial^2}{\partial x \partial y}$ are computed for every inner node, together with the error with respect to the exact result, which is obtained by direct differentiation of the polynomials in $\mathcal{B}$, namely

$$\partial_x(x, x^2, xy) = (1, 2x, y), \quad \partial_y(y, xy, y^2) = (1, x, 2y),$$

$$\partial_{xx}(x^2) = 2, \quad \partial_{yy}(y^2) = 2, \quad \partial_{xy}(xy) = 1,$$

for each $(x, y) \in \Omega$, with all remaining derivatives identically zero. For each polynomial in $\mathcal{B}$, the maximum of these errors over the cloud of points is reported in Table 1, except for 1, as all the results are directly 0. All computations are performed in MATLAB on a Dell XPS 13 9370, Intel Core i7-8550U CPU 1.80 GHz, 1.99 GHz.

As expected, the outcome of the errors is nearly zero for all cases, with values that lie between 10^{-16} and 10^{-14}, which corresponds to standard floating-point round-off in double precision (MATLAB `eps` $= 2.2204 \cdot 10^{-16}$). The results confirm the exactness, up to machine precision, of the second-order least-squares partial derivative formulae obtained through the GFD method for such polynomials of degree up to two.

Having tested the reconstruction of the partial derivatives, we now turn to the numerical resolution of system (1) in order to study the transient regime before the PDE dynamics – governed by the eventual spatial homogeneity of the source f –, effectively reduce to those of the associated ODE system, as well as its convergence and periodicity properties, for long timescales.

5.2. Numerical simulations of the system

We next carry out the numerical integration of system (1), using the GFD scheme (20). In order to obtain certain spatial structure before the system eventually homogenizes, we consider the following pair of initial values

$$u(x, y, 0) = 10e^{-8\left((x-0.5)^2+(y-0.5)^2\right)}, \quad v(x, y, 0) = 2y^2\big(1 + \sin(4\pi x)\big). \tag{23}$$

Thus, the initial population of the species is mostly concentrated around the center of the domain, with a maximum value of 10, much above 1, the normalized carrying capacity of the logistic term. In turn, the substance concentration presents oscillations in the x direction, with a quadratic increase from 0 to 1 in the y direction, attaining its maximum at the points $(1/8, 1)$ and $(5/8, 1)$, with a value of 4. The graph of both initial values over Ω is represented in Fig. 14.

Table 1
Maximum error over the inner nodes of the irregular discretization for each spatial derivative of the polynomials in $\mathcal{B}$ except for 1.

Polynomial	Maximum error for each derivative				
	$\frac{\partial}{\partial x}$	$\frac{\partial}{\partial y}$	$\frac{\partial^2}{\partial x^2}$	$\frac{\partial^2}{\partial y^2}$	$\frac{\partial^2}{\partial x \partial y}$
x	$5.551 \cdot 10^{-16}$	$2.637 \cdot 10^{-16}$	$8.660 \cdot 10^{-15}$	$8.882 \cdot 10^{-15}$	$5.329 \cdot 10^{-15}$
y	$4.718 \cdot 10^{-16}$	$6.661 \cdot 10^{-16}$	$7.550 \cdot 10^{-15}$	$2.132 \cdot 10^{-14}$	$2.043 \cdot 10^{-14}$
x^2	$1.110 \cdot 10^{-15}$	$4.996 \cdot 10^{-16}$	$2.842 \cdot 10^{-14}$	$2.309 \cdot 10^{-14}$	$1.243 \cdot 10^{-14}$
y^2	$4.996 \cdot 10^{-16}$	$1.332 \cdot 10^{-15}$	$1.332 \cdot 10^{-14}$	$3.908 \cdot 10^{-14}$	$1.910 \cdot 10^{-14}$
xy	$7.772 \cdot 10^{-16}$	$9.992 \cdot 10^{-16}$	$3.419 \cdot 10^{-14}$	$3.197 \cdot 10^{-14}$	$1.421 \cdot 10^{-14}$

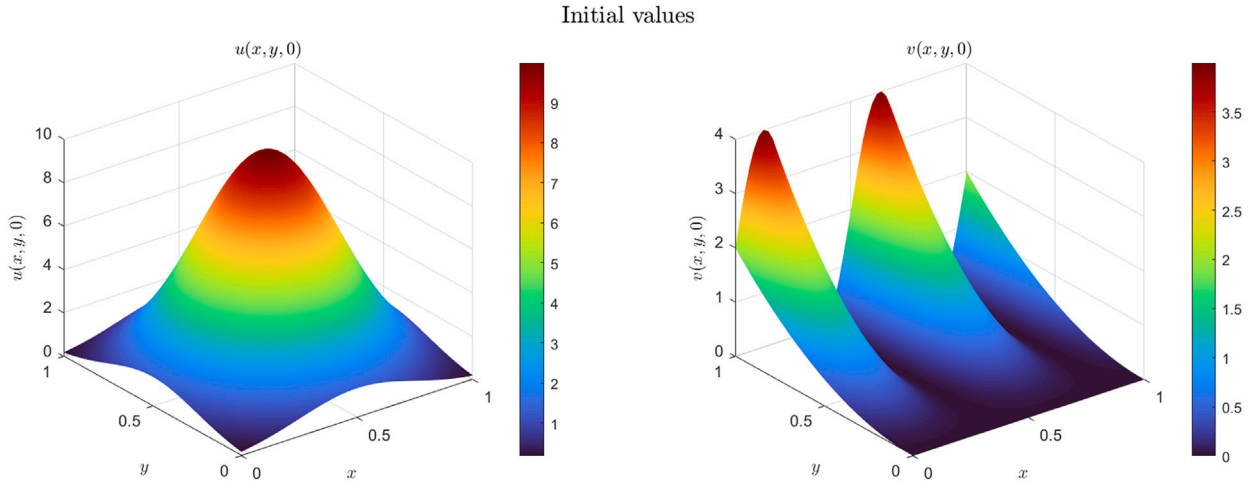

Fig. 14. Initial values (23) for the numerical simulations.

For the simulations, we consider the following parameter set

$$D = 0.5, \quad \chi = 5, \quad r = 1, \quad a = \{0, 0.5\}, \tag{24}$$

corresponding to a strong chemotaxis response (10 times the diffusion coefficient of the species). For a – the self-production rate of the substance by the species – we consider both the case $a = 0$, resulting in an uncoupled system, and the strictly positive $a = 0.5$ representing a lethal byproduct self-produced by the species.

Regarding the external supply of the lethal chemorepellent, we consider a persistent periodic term with a time-decaying spatial perturbation

$$f(x, y, t) = M \cdot (1 + \cos(t)) + e^{-\alpha t} q(x, y), \tag{25}$$

for certain $M, \alpha > 0$ and $q \in L^1(\Omega) \cap L^\infty(\Omega)$, which converges in the sense of (7) to

$$\tilde{f}(t) = M \cdot (1 + \cos(t)), \tag{26}$$

to match the numerical examples considered for the ODE system in Section 3. With this choice of $\tilde{f}$, the value of $r_{\min}$ in (11) that determines the periodicity threshold for the case $a = 0$ – and possibly as well in the coupled case $a > 0$, as the experiments in Section 3 seem to indicate– is

$$r_{\min} = M.$$

Moreover, for $a = 0.5$, the value of $r_{\min,a}$ in (9), computed through a, $\tilde{f}$, $u(x, y, 0)$ and $v(x, y, 0)$, corresponds here to

$$\begin{aligned} r_{\min,a} &= \max\left\{ \int_\Omega v(x,y,0),\ a \cdot \max\left\{ \int_\Omega u(x,y,0), 1 \right\} + \|\tilde{f}\|_{L^\infty(0,\infty)} \right\} \\ &= \max\left\{ \frac{2}{3}, 0.5 \cdot \max\left\{ \frac{5\pi}{4} \mathrm{erf}(\sqrt{2})^2, 1 \right\} + 2M \right\} \approx 1.7888 + 2M. \end{aligned}$$

Motivated by the results from Section 3, for the case with positive a, we expect that for any $M > 0$ such that $r > r_{\min} = M$, the solution $(\tilde{u}, \tilde{v})$ to the ODE system (3) will be asymptotically periodic, and in particular bounded from below by a positive constant. Thus, the convergence of the solution (u, v) of the full PDE system (1) to $(\tilde{u}, \tilde{v})$ will still hold, even if $r \not> r_{\min,a}$. Moreover, we will test if for a large enough $M > 0$ (this is $M = r_{\min} \geq r$), (u, v) still converges to the time-decaying $(\tilde{u}, \tilde{v})$.

For this reason, we consider the following cases for the simulations:

1. The case $a = 0$ with $M = r_{\min} < r$, to verify the convergence to the asymptotically periodic solution $(\tilde{u}, \tilde{v})$ of the uncoupled version of system (3).
2. The previous case with $a = 0.5 > 0$, and $M > 0$ satisfying $M = r_{\min} < r < 1.7888 + 2M = r_{\min,a}$, to test if $(\tilde{u}, \tilde{v})$ inherit the periodicity of $\tilde{f}$ and $\tilde{u}$ is bounded from below – as expected from Section 3 – and thus if (u, v) converges to $(\tilde{u}, \tilde{v})$.
3. The case with a large enough $M > 0$ such that $M = r_{\min} \geq r$, with both $a = 0$ and $a = 0.5 > 0$, to study if (u, v) still converges to $(\tilde{u}, \tilde{v})$, leading to the extinction of the population.

For all the simulations, a time step of $\Delta t = 10^{-3}$ is selected, which meets the convergence condition from 4.2. The computations are performed on both the regular and irregular discretizations of Ω shown in Fig. 13 and it is checked that the results are within an error tolerance from each other. For brevity reasons, only the results obtained with the irregular cloud of points are shown.

5.2.1. *Case 1:* $a = 0$, $M < r$

For this case, we numerically solve the uncoupled version of system (1) with a small enough supply rate, such that the threshold for periodicity is met. We select for instance the value $M = 0.5 < 1 = r$. Thus, as for the $\tilde{f}$ selected in (26), $r_{\min} = M$, the condition $r_{\min} < r$ ensures that

the solution $\tilde{u}$ to the uncoupled version of system (3) is both bounded from below by a strictly positive constant and asymptotically periodic. This guarantees that (u, v) converges to $(\tilde{u}, \tilde{v})$ in the sense of (10).

For the external supply of the substance f given in (25), we take for instance

$$q(x, y) = 0.1 \cdot \Big(1 + \cos(\pi x) \cdot \cos(\pi y)\Big), \quad \alpha = 2, \tag{27}$$

to represent a fast decaying perturbation that distributes more supply near the corners of the domain $(0, 0)$ and $(1, 1)$ and none around $(0, 1)$ and $(1, 0)$.

Using initial values (23) and parameters (24) with $a = 0$, we numerically solve system (1) using the GFD scheme (20). The obtained numerical solution is plotted at different time instants in Fig. 15.

As can be seen, after the initial values depicted in Fig. 14, the top panel in Fig. 15 represents the numerical solution at $t = 0.05$. With respect to u, the strong negative chemotactic effect (as $\chi = 5$) drives the solution towards $y = 0$ and $x = 1$, the areas where the initial concentration of the lethal repellent was at its lowest. Concerning v, diffusion (with a normalized coefficient of 1) quickly distributes the chemical, homogenizing the initial oscillations that the initial $v(x, y, 0)$ presented.

The second panel shows the solution profiles at $t = 0.5$. The first relevant aspect concerning u is the considerable change on its scale. While the initial value $u(x, y, 0)$ presented a global maximum at the center of the domain with a total population density of 10, this has been greatly reduced during these instants due to the strong logistic term, which has a maximum normalized capacity of 1. Moreover, diffusion has smoothened the local maxima appearing on the previous panel. The effect of the perturbed supply is now visible on v, as we recall that the perturbation q in (27) accounts for a greater source of chemical on the corners $(0, 0)$ and $(1, 1)$, and none (thus only yielding the baseline supply of $\tilde{f}$) for $(0, 1)$ and $(1, 0)$, which matches the change in shape with respect to the previous profile.

At $t = 1$, represented on the third panel, this spatial effect of the source is intensified, with v attaining maxima at $(0, 0)$ and $(1, 1)$, and minima at $(0, 1)$ and $(1, 0)$. The resulting chemotactic response of the species leads to a redistribution of u towards those regions of less substance concentration. Such redistribution is completed by $t = 2$, as can be seen on the bottom panel. The difference in scale is however noticeable, as with time, solutions become flatter, as a result to their convergence to $(\tilde{u}, \tilde{v})$, the solution to the associated ODE system (3) with initial values (8). From then on, the values of u and v are mainly driven by the oscillations in $\tilde{f}$.

To better visualize this convergence to $(\tilde{u}, \tilde{v})$, we plot in red the temporal evolution of u and v for instance at the center of the domain, together with $(\tilde{u}, \tilde{v})$ in dashed blue in Fig. 16. For reference, the graph of $\tilde{f}(t)$ is also added on the same panel as v and $\tilde{v}$.

We see how after $t = 6$ both curves are nearly identical, illustrating how the dynamics of the full PDE model effectively reduce to those of the associated ODE system. For better visibility, the plot of the values of u and $\tilde{u}$ on the top panel, are zoomed in to avoid including the initial value of $u(0.5, 0.5, 0) = 10$ in order to show the convergence more clearly.

For this case, as the supply is comparatively small, with M satisfying $r > r_{\min} = M$, the resulting solution $(\tilde{u}, \tilde{v})$, to system (3) is asymptotically periodic, as can be inferred from Fig. 16, resulting in periodic dynamics as well for (u, v). In this periodic regime, the phase of the u and v is shifted. Whenever $\tilde{v}$ attains a local minimum due to a decreasing supply, such low concentration of the lethal substance fosters the growth of $\tilde{u}$, the population density. This growth in $\tilde{u}$ occurs while the substance supply is increasing, eventually generating a strong lethal response, which in turn causes $\tilde{u}$ to decrease.

There is also a visible phase shift between the supply $\tilde{f}$ its effect on $\tilde{v}$. To analyze this delay, in this case $a = 0$ system (3) is uncoupled, with the second equation being $\tilde{v}' = -\tilde{v} + \tilde{f}(t)$, which can be explicitly solved, yielding

$$\tilde{v}(t) = e^{-t} \cdot \tilde{v}(0) + \int_0^t \tilde{f}(s)\, e^{-(t-s)}\, ds. \tag{28}$$

If $\tilde{f}(t) = M \cdot \big(1 + \cos(At + B)\big)$ as in our case, with period $T = 2\pi/A$, this leads to

$$\begin{aligned} y(t) &= C_1 e^{-t} + M + \frac{M}{1 + A^2} \left[\cos(At + B) + A \sin(At + B)\right] \\ &= C_1 e^{-t} + M + \frac{M}{\sqrt{1 + A^2}} \cos\big(At + B - \arctan(A)\big). \end{aligned}$$

for $C_1 := \tilde{v}(0) - M - \dfrac{M(\cos(B) + A \sin(B))}{1 + A^2}$.

Thus, the substance concentration $\tilde{v}$ experiments a delay of $\arctan(A)$ with respect to $\tilde{f}$. This delay increases with the frequency A of the supply, with a limit of $\pi/2$. Moreover, the maximum concentration of the substance is $M + \dfrac{M}{\sqrt{1 + A^2}}$. For our particular case $M = 0.5$, $A = 1$, $B = 0$, this results in the observed delay of $\arctan(1) = \pi/4 \approx 0.785$, and the maximum substance concentration of approximately 0.854.

It is thus the degradation term $-\tilde{v}$ appearing on the right hand side of its ODE that causes this delay. This can be seen by means of the integrand $\tilde{f}(s)e^{-(t-s)}$ on (28). Interpreting the integral as an weighted average of past values of the source $\tilde{f}$. Hence $\tilde{v}$ cannot follow $\tilde{f}$ instantaneously, as past values of $\tilde{f}$ still contribute to its dynamics, although with exponentially decaying weight.

5.2.2. Case 2: $a > 0$, $M = r_{\min} < r < 1.7888 + 2M = r_{\min,a}$

Now, we reproduce the previous numerical simulations but with the strictly positive $a = 0.5$. From the modeling point of view, this represents a non-negligible self production of the lethal chemical by the individuals of the biological species.

Again, we consider the remaining parameters as in (24) and the expression for f given in (25), with $\tilde{f}$ in (26) as well as q and α from (27). The same initial values $u(x, y, 0)$ and $v(x, y, 0)$ from (23) are used. With respect to M, the scale factor of the supply, we also keep $M = 0.5$, as it satisfies

$$0.5 = M = r_{\min} < r = 1 < 1.7888 + 2M = r_{\min,a} = 2.7888.$$

We recall that this case was interesting, as in principle $r < r_{\min,a}$ and hence $\tilde{u}$ dos not necessarily have a strictly positive lower bound, which does not allow us to obtain the convergence result (10). However, the experiments from Section 3 seem to indicate that $r > r_{\min}$ is enough to obtain a strictly positively bounded and asymptotically periodic $\tilde{u}$. Therefore, we expect to be able to obtain similar convergence results for (u, v), as well as asymptotic periodicity.

Solving the system numerically with the scheme (20), we plot solution profiles at different time instants in Figs. 17 and 18.

First, for Fig. 17, on the top panel corresponding to $t = 0.05$, we find very similar values to those obtained in Fig. 16 for $a = 0$, as the effect of self production of the substance is still small. However, it is indeed visible, as the lowest values of v are approximately 0.4, greater than the previous ones, which were close to 0.2. Next, we include an intermediate time point $t = 0.225$, on the middle row, which was not that relevant in the previous case. This time, we can observe how – although considerably reduced as a result of the regulation by the logistic term – the larger population density u close to $y = 0$ results in an increase of the concentration of the chemical near that region, as a consequence of its self-production. This is further intensified at $t = 0.5$, on the bottom panel, where both components u and v indeed present similar shapes, with their maximum values around $y = 0$.

Subsequent time profiles are depicted in Fig. 18. The top panel corresponds to $t = 0.75$, where effect of chemotaxis has already distributed the population away from the previous higher concentrations of the chemical. The effects of the perturbed source start to be visible at this point, with v having its maximum at $(0, 0)$, and a considerable increase around $(1, 1)$. This spatial structure ultimately prevails, as can

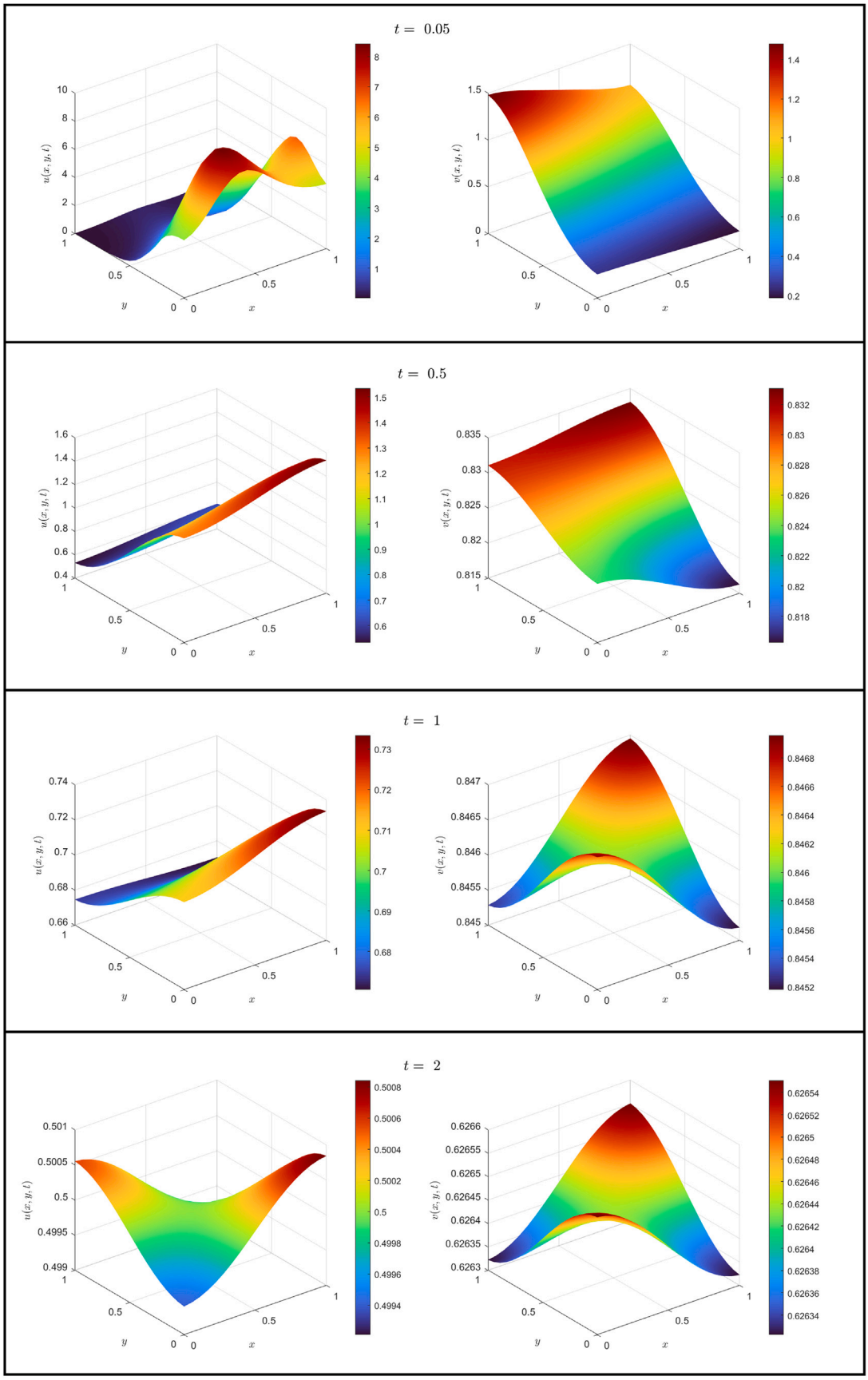

Fig. 15. Different time profiles of the numerical solution (u, v) to system (1) with initial values (23) and parameters (24) ($a = 0$). On each panel, u is represented on the left and v on the right.

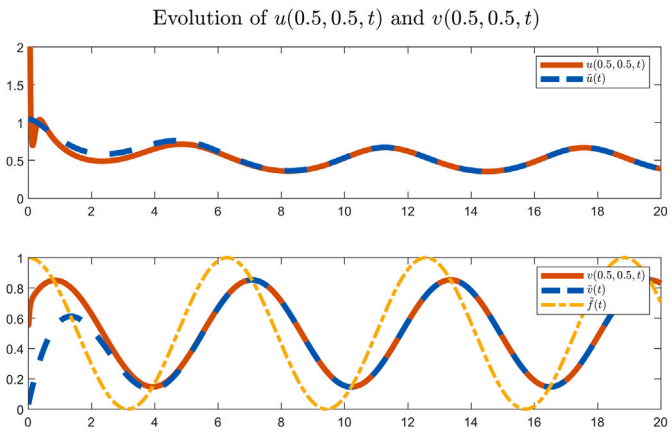

Fig. 16. Convergence of (u, v), the solution to system (1) with initial values (23) and parameters (24) ($a = 0$) to $(\tilde{u}, \tilde{v})$, the solution to the associated ODE system (3) with initial values (8).

be seen for $t = 1$ on the middle row, and $t = 2$ on the bottom. As in the previous case, the solution quickly flattens, which produces no significant differences on the value of au over the domain. This prevents further redistribution of the species, and thus the solution seems to preserve its shape over time, while oscillating due to the periodicity in $\tilde{f}$ and continuing to flatten.

To assess the convergence to the solutions $(\tilde{u}, \tilde{v})$ of the associated ODE system (3), the evolution of (u, v) again at $(0.5, 0.5)$ is depicted in Fig. 19, together with $(\tilde{u}, \tilde{v})$, as well as $\tilde{f}$ for reference.

As in the previous case $a = 0$, after $t = 6$ both curves are nearly identical, obtaining the expected convergence to $(\tilde{u}, \tilde{v})$. In fact, $(\tilde{u}, \tilde{v})$ is seen to be bounded from below by a positive constant and asymptotically periodic, as expected from the results obtained in Section 3, as $r > r_{\min}$, even if $r \not> r_{\min,a}$. Upon comparison with Fig. 16 from the case $a = 0$, the main difference lies on the values of the v component. As in this case a is positive, the self-production of the substance by the species results in greater values of v than in the previous case with $a = 0$. In particular, the local maxima of v here are above 1, while Fig. 16 showed values barely above 0.8.

Regarding the phase shift in $\tilde{v}$ with respect to $\tilde{f}$, this time the nonlinear coupling due to $a > 0$ prevents us from obtaining an explicit expression for $\tilde{v}$ to analyze. Estimating the delay from the numerical resolution yields approximately 0.669, which is arguably less than $\pi/4 \approx 0.785$, the previous delay from the uncoupled case. This is a result of the positive self-production term $+a\tilde{u}$ slightly compensating the decay term $-\tilde{v}$, responsible for the delay. However, no analytical characterization of this phase shift has been found so far.

5.2.3. Case 3: $M = r_{\min} \geq r$

Lastly, we numerically solve system (1) with a value of M large enough to compensate the logistic growth on the ODE system (3). In particular, as for $\tilde{f}$ in (26) one has $r_{\min} = M$, considering $M \geq r$, implies that $\tilde{u}$ decays in time (at least for the case $a = 0$, and possibly as well for $a > 0$, as suggested by the results from Section 3). This falls outside the framework of [11], where the analysis relies on a strictly positive lower bound for $\tilde{u}$, which does not exist on this case. Thus, our goal is to determine whether this type of source term can drive the population density u to extinction while continuing to converge to $\tilde{u}$.

Taking for instance $M = 1.5$, which exceeds $r = 1$, we compute the numerical solution to the system under the previous conditions, with initial values (23) and parameters (24), for both the coupled and decoupled cases $a = 0$ and $a = 0.5 > 0$. For brevity reasons, we only include the plots of the evolution of (u, v) at the center of the domain, which are represented in Fig. 20.

On both cases, the evolution curves rapidly converge to $(\tilde{u}, \tilde{v})$, which shows the expected time decay in the $\tilde{u}$ component. Thus, at least for this case, not only does the supply of the substance drive u to extinction, but it also does it with the same dynamics as the time-decaying $\tilde{u}$. As in the previous experiments, the difference between the case $a = 0$ and $a > 0$ is mainly notable in the v component of the solutions, producing larger values for $a > 0$ as a result of the self-production of the substance.

6. Optimal control formulation and pontryagin-based analysis for the ODE system

Lastly, motivated by these last results obtained for a large value of M, we formulate an optimal control problem associated to system (1), where we interpret the source function f as a control.

Assume, as mentioned in the Introduction, that the population species u represents a proliferating harmful bacterial species, and that the chemical substance v in an antibiotic. By renaming the previous supply $f(\boldsymbol{x}, t)$ by $\alpha(\boldsymbol{x}, t)$, we consider that the antibiotic can be freely supplied according to α, within a certain range $[\alpha_{\min}, \alpha_{\max}]$, with $0 \leq \alpha_{\min} < \alpha_{\max}$. Hence, for a given $t_f > 0$, we consider the following optimal control problem.

$$\begin{cases} \min\limits_{\alpha \in A_{ad}} \mathcal{J}[\alpha, u, v] := \|u(\cdot, t_f)\|^2_{L^2(\Omega)} + \lambda \|\alpha\|^2_{L^2\left(\Omega \times (0,t_f)\right)}, \\ \text{subject to:} \\ \dfrac{\partial u}{\partial t} = D\Delta u + \chi \nabla \cdot (u \nabla v) + ru(1-u) - uv, & \boldsymbol{x} \in \Omega,\ t \in (0, t_f), \\ \dfrac{\partial v}{\partial t} = \Delta v + au - v + \alpha(\boldsymbol{x}, t), & \boldsymbol{x} \in \Omega,\ t \in (0, t_f), \end{cases} \tag{29}$$

for a given $\lambda > 0$, together with Neumann homogeneous boundary conditions and nonnegative initial values for u and v, as set in (2). The set A_{ad} represents the space of admissible controls, yet to be specified.

The functional $\mathcal{J}$ represents the sum of the bacterial population density at $t = t_f$ plus the total supply of the antibiotic, weighted by the regularization parameter λ. We hence intend to minimize the final number of bacteria, without providing too much antibiotic, which may be harmful on its own.

The mathematical analysis of optimal control problems of Keller–Segel type equations is particularly involved and exceeds the scope of this work (for more information and references of related optimal control problems for chemotaxis-consumption models, see the review [24]). For out study, however, we particularize the analysis for spatially homogeneous controls, $\alpha(\boldsymbol{x}, t) \equiv \alpha(t)$, and employ the convergence strategy to $(\tilde{u}, \tilde{v})$. to simplify the problem. Thus, we define the space of admissible controls as

$$\begin{aligned} A_{ad} &:= \left\{ \alpha \in L^2\left(\Omega \times (0, t_f)\right),\ \alpha(\boldsymbol{x}, t) \equiv \alpha(t),\ \alpha_{\min} \leq \alpha(t) \leq \alpha_{\max} \right\} \\ &= \left\{ \alpha \in L^2(0, t_f),\ \ \alpha_{\min} \leq \alpha(t) \leq \alpha_{\max} \right\}. \end{aligned} \tag{30}$$

Under this spatial homogeneity hypothesis, based on the previous numerical experiments, we expect that for a sufficiently large t_f, $u(\boldsymbol{x}, t_f) \approx \tilde{u}(t_f)$ for any $\boldsymbol{x} \in \Omega$. We can therefore approximate functional $\mathcal{J}$ as

$$\mathcal{J} = \|u(\cdot, t_f)\|^2_{L^2(\Omega)} + \lambda \|\alpha\|^2_{L^2\left(\Omega \times (0,t_f)\right)} \approx |\Omega| \cdot \tilde{u}(t_f)^2 + \lambda |\Omega| \cdot \|\alpha\|^2_{L^2(0,t_f)} =: |\Omega| \cdot \tilde{\mathcal{J}}.$$

So, as a heuristic approximation to the solution of (29), we solve the spatially homogeneous problem

$$\begin{cases} \min\limits_{\alpha \in A_{ad}} \tilde{\mathcal{J}}[\alpha, \tilde{u}, \tilde{v}] = \tilde{u}(t_f)^2 + \lambda \displaystyle\int_0^{t_f} \alpha(t)^2 \, dt \\ \text{subject to:} \\ \dfrac{d\tilde{u}}{dt} = r\tilde{u}(1-\tilde{u}) - \tilde{u}\,\tilde{v}, & t \in (0, t_f) \\ \dfrac{d\tilde{v}}{dt} = a\tilde{u} - \tilde{v} + \alpha(t), & t \in (0, t_f), \end{cases} \tag{31}$$

under initial values

$$\tilde{u}(0) = \frac{1}{|\Omega|} \int_\Omega u(\boldsymbol{x}, 0)\, d\boldsymbol{x}, \quad \tilde{v}(0) = \frac{1}{|\Omega|} \int_\Omega v(\boldsymbol{x}, 0)\, d\boldsymbol{x}.$$

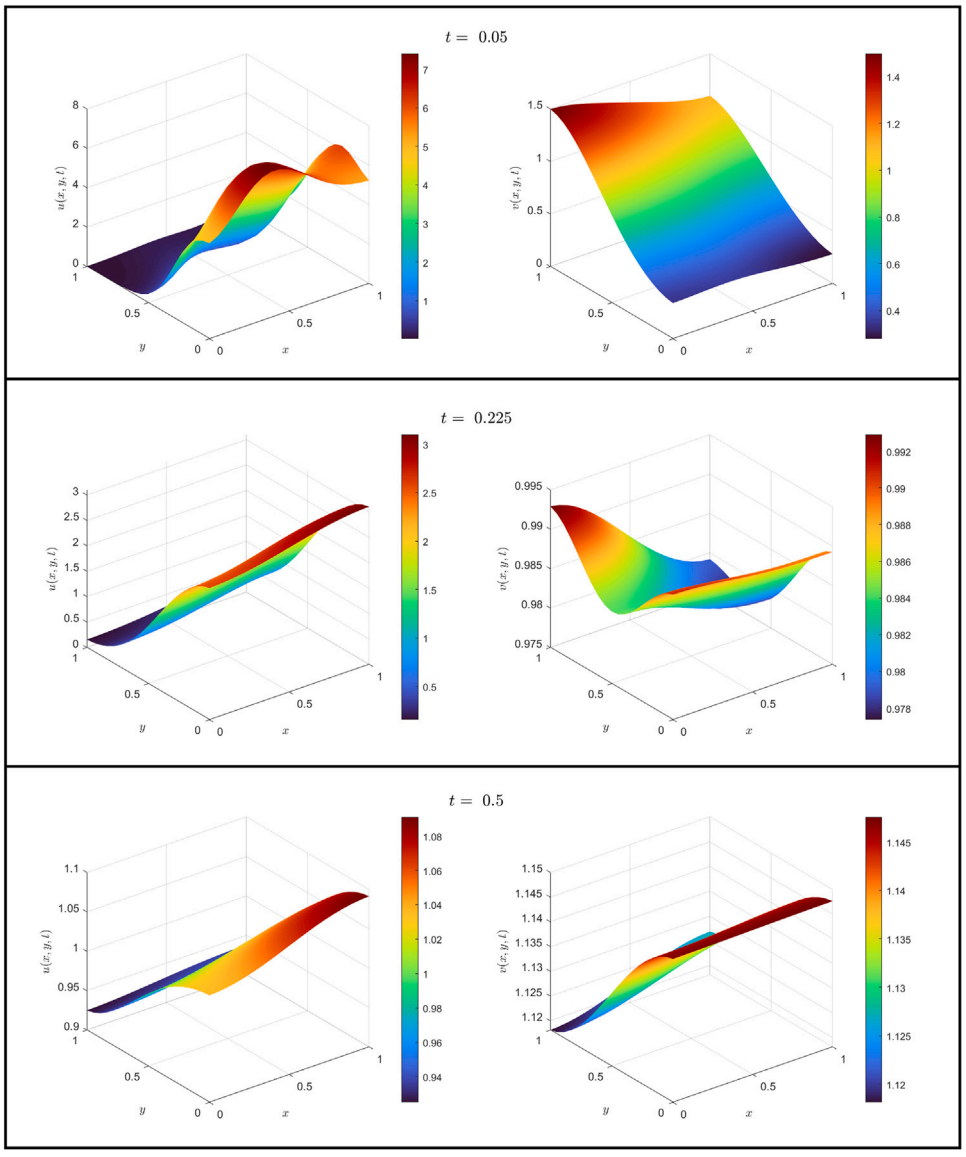

Fig. 17. Different time profiles of the numerical solution (u, v) to system (1) with initial values (23) and parameters (24) ($a = 0.5$). On each panel, u is represented on the left and v on the right.

As opposed to problem (29), the minima of (31) can be easily characterized by means of Pontryagin's minimum principle [25]. In particular, by introducing two co-states p_1 and p_2 and considering the Hamiltonian

$$H(\tilde{u}, \tilde{v}, p_1, p_2, \alpha) := p_1\left[r\tilde{u}(1-\tilde{u}) - \tilde{u}\,\tilde{v}\right] + p_2\left[a\tilde{u} - \tilde{v} + \alpha\right] + \lambda\alpha^2$$

one obtains the necessary conditions for the optimal $(\tilde{u}^*, \tilde{v}^*, p_1^*, p_2^*, \alpha^*)$ for $\mathcal{J}$ as the solution to the following boundary value problem

$$\begin{cases} \dfrac{d}{dt}(\tilde{u}^*) = \dfrac{dH}{dp_1} = r\tilde{u}^*(1-\tilde{u}^*) - \tilde{u}^*\,\tilde{v}^*, & \dfrac{d}{dt}(p_1^*) = -\dfrac{dH}{d\tilde{u}} \\ & \quad = p_1^*(2r\tilde{u}^* + \tilde{v}^* - r) - ap_2^*, \\ \dfrac{d}{dt}(\tilde{v}^*) = \dfrac{dH}{dp_2} = a\tilde{u} - \tilde{v} + \alpha(t), & \dfrac{d}{dt}(p_2^*) = -\dfrac{dH}{d\tilde{v}} = p_1^*\tilde{u}^* + p_2^*, \\ \tilde{u}^*(0) = \dfrac{1}{|\Omega|}\displaystyle\int_\Omega u(\boldsymbol{x}, 0), \quad \tilde{v}^*(0) = \dfrac{1}{|\Omega|}\int_\Omega v(\boldsymbol{x}, 0), & p_1^*(t_f) = 2\tilde{u}^*(t_f), \quad p_2^*(t_f) = 0. \end{cases} \tag{32}$$

where α^* is characterized by the minimum property

$$H\left(\tilde{u}^*(t), \tilde{v}^*(t), p_1^*(t), p_2^*(t), \alpha^*(t)\right) = \min_{\alpha\in[\alpha_{\min}, \alpha_{\max}]} H\left(\tilde{u}^*(t), \tilde{v}^*(t), p_1^*(t), p_2^*(t), \alpha\right)$$
$$= \max\left\{\alpha_{\min},\ \min\left\{-\frac{p_2^*}{2\lambda},\ \alpha_{\max}\right\}\right\} \quad \text{for all } t \in (0, t_f). \tag{33}$$

In practice, different numerical methods are available for the resolution of problem (32)–(33). For the purpose of our work, we exemplify a numerical example using the Forward-Backward Sweep method (for a description of the method and analysis of the convergence see [26–28]).

6.1. Numerical example

To test the method in order to find an approximation to the solution of (29), we consider again for instance the same domain as in Section 5, $\Omega = [0, 1]^2$, and the same parameter set as in (24), with the positive choice of a, this is

$$D = 0.5, \quad \chi = 5, \quad r = 1, \quad a = 0.5. \tag{34}$$

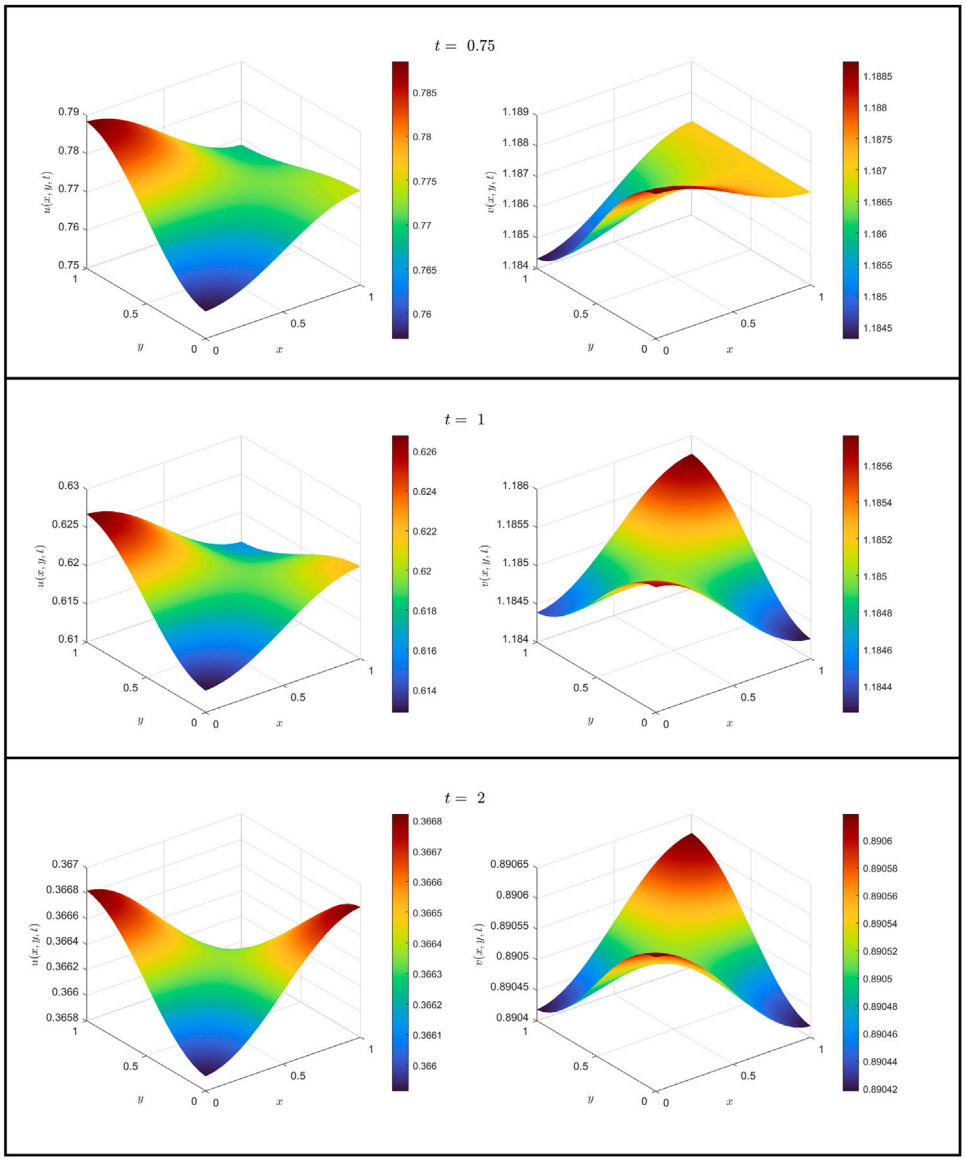

Fig. 18. Further time profiles of the numerical solution (u, v) to system (1) with initial values (23) and parameters (24) ($a = 0.5$). Again, on each panel, u is represented on the left and v on the right.

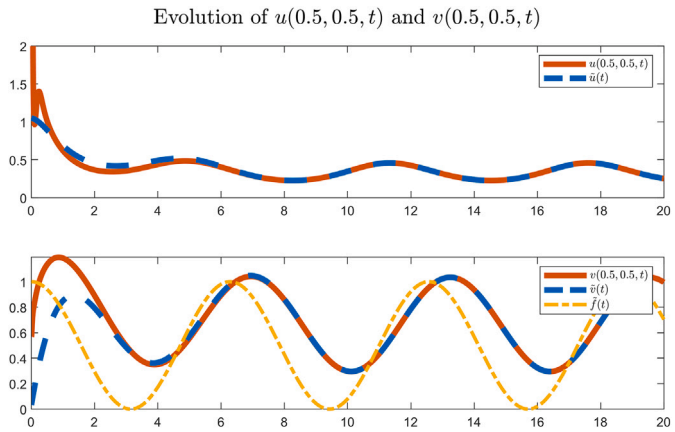

Fig. 19. Convergence of (u, v), the solution to system (1) with initial values (23) and parameters (24) ($a = 0.5$) to $(\bar{u}, \bar{v})$, the solution to the associated ODE system (3) with initial values (8).

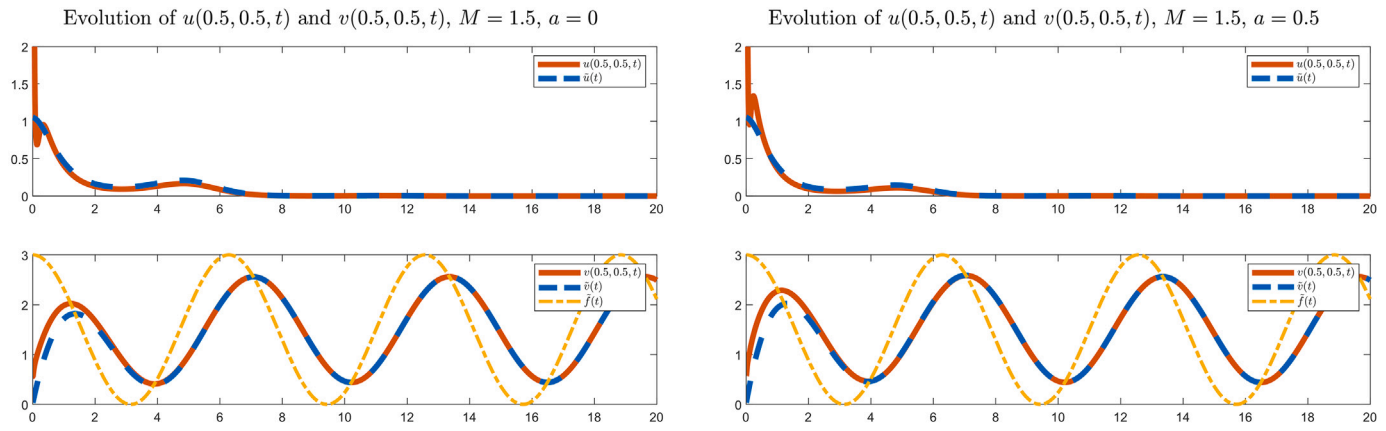

Fig. 20. Convergence of (u, v), to $(\tilde{u}, \tilde{v})$ for $M = 1.5 > r$ in the case $a = 0$ (left) and $a = 0.5$ (right).

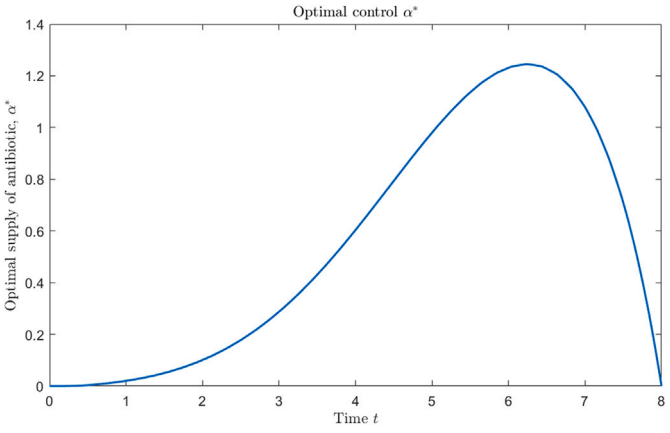

Fig. 21. Obtained optimal control for the ODE problem (31) with initial values $\tilde{u}(0) = 0.5$, $\tilde{v}(0) = 0$ and parameters given in (34) and (36).

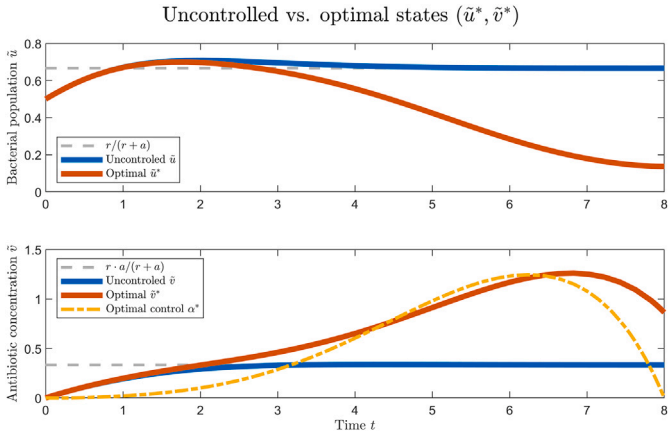

Fig. 22. Uncontrolled and optimal states of the ODE problem (31) Steady states for the uncontrolled system and optimal control included for reference.

As initial values however, we take a population density such that $\frac{1}{|\Omega|}\int_\Omega u(\boldsymbol{x},0)\,d\boldsymbol{x} = 0.5$, so that over Ω, the bacteria have proliferated up to a half of the carrying capacity, and the initial antibiotic concentration as zero. For instance, we consider

$$u(\boldsymbol{x},0) = \frac{3}{2}\cdot\big(x(1-x)+y(1-y)\big), \quad v(\boldsymbol{x},0)\equiv 0, \tag{35}$$

where the bacterial population density achieves a maximum at the center of the domain, with a value of 0.75 and vanishes on $\partial\Omega$. As parameters for the control, we consider

$$\alpha_{\min} = 0, \quad \alpha_{\max} = 5, \quad \lambda = 0.01, \tag{36}$$

and a time horizon of $t_f = 8$. Hence, we numerically solve the ODE optimal control problem (32)–(33) by means of a Forward-Backward Sweep method, and use the obtained α^* to solve system (1) with the obtained control, i.e. with $f(\boldsymbol{x},t) = \alpha^*(t)$. For the Forward-Backward Sweep, an initial control of $\alpha(t) \equiv 1$ is considered, and the algorithm is stopped once a maximum difference of less than 10^{-4} is obtained between two successive computed controls.

The obtained optimal control α^* is represented in Fig. 21. Starting from 0, the optimal supply of antibiotic starts increases with time, with a very slow rate at the beginning, until reaching a maximum near $t = 6$, with a value slightly over 1.2. For then on, the supply decreases until reaching 0 again at t_f.

The optimal states $(\tilde{u}^*, \tilde{v}^*)$, along with the uncontrolled solution associated to $\alpha \equiv 0$ are depicted in Fig. 22. The steady states $\left(\frac{r}{r+a}, \frac{r\cdot a}{r+a}\right)$ for the uncontrolled case are also represented in gray dashed line.

As can be seen on the top panel, during the first two time units both the uncontrolled $\tilde{u}$ and the optimal $\tilde{u}^*$ are nearly identical, as the obtained α^* is still relatively small. During this time interval, the bacterial population has nearly reached the maximum possible spread that the system can sustain, given by the steady state $r/(r+a)$. However, as more antibiotic is eventually supplied, the red curve corresponding to the controlled solution decreases, as the lethality affects the bacteria, reducing the proliferation of the species. At t_f, the final value of the optimal state is $\tilde{u}^*(8) \approx 0.137$, not only significantly below the value of the uncontrolled $\tilde{u}(8)$, but also considerably its initial value, $\tilde{u}^*(0) = 0.5$. Thus, at least on the ODE level, the control succeeds in preventing the bacterial proliferation.

With respect to the $\tilde{v}$ component, the uncontrolled and the optimal state are represented on the bottom panel, as well as the optimal control α^* for reference. On the first instants, it is mainly the self production of antibiotic by the bacteria that makes $\tilde{v}^*$ increase, as α^* is nearly 0. This is again visible by the scarce difference between the uncontrolled and the optimal values. After $t = 2$, this difference is intensified, as the optimal supply of antibiotic increases. Lastly, after $t = 7$, the drop in α^* translates into a delayed decrease (caused by the decay term) of $\tilde{v}^*$.

Lastly, we numerically solve system (1) with $f(\boldsymbol{x},t) = \alpha^*(t)$ to study the effect of this spatially homogeneous control over the full PDE system. Fig. 23 shows the final solution profiles at $t = t_f$, while in Fig. 24 the evolution of (u, v) at the center of the domain is represented along with $(\tilde{u}^*, \tilde{v}^*)$.

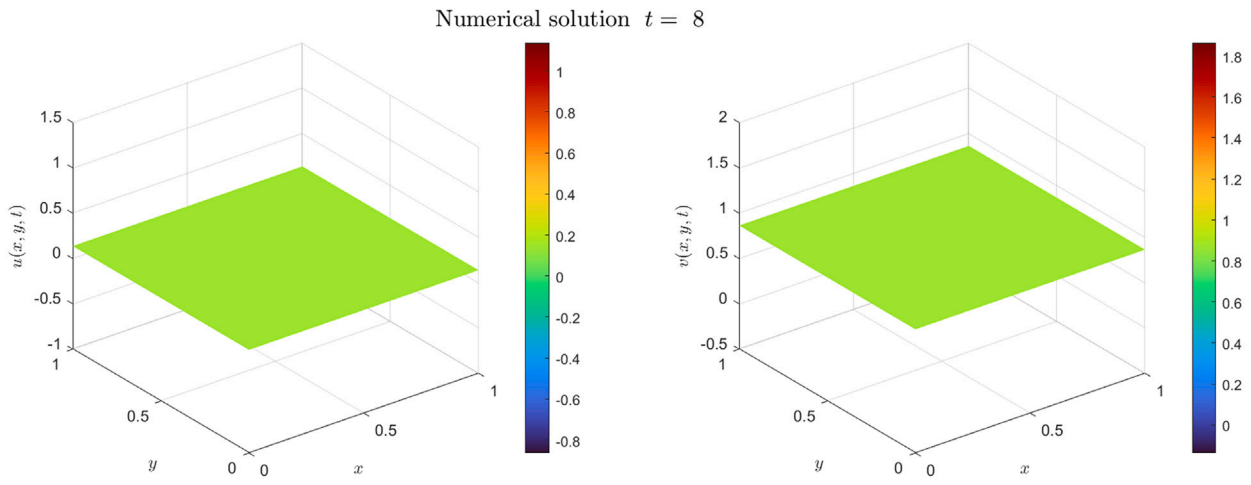

Fig. 23. Numerical solution (u, v) to system (1) with $f(\boldsymbol{x}, t) = \alpha^*(t)$, the optimal control from the ODE problem (31), evaluated at $t = t_f = 8$.

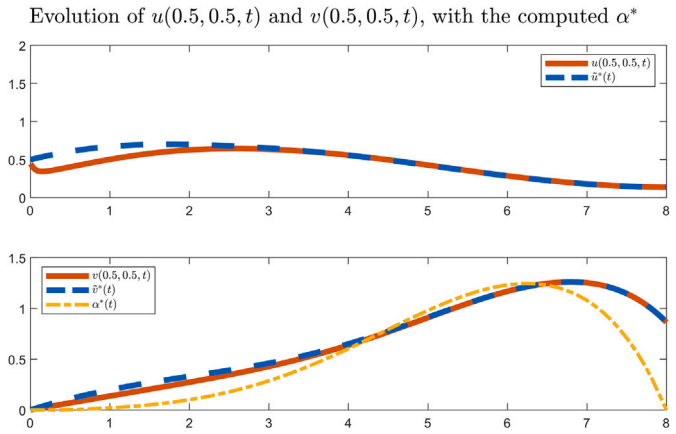

Fig. 24. Evolution of (u, v) at $(0.5, 0.5)$, along with $(\tilde{u}^*, \tilde{v}^*)$, the optimal states of problem (31).

As can be seen, the convergence of the solution (u, v) of the full PDE system (1), to $(\tilde{u}^*, \tilde{v}^*)$, the optimal states of the optimal control problem for the ODE system (3) still holds. Indeed, at the final time $t_f = 8$, Fig. 23 shows how both u and v have completely flattened, with $\big(u(x, y, t_f), v(x, y, t_f)\big) \approx \big(\tilde{u}^*(t_f), \tilde{v}^*(t_f)\big)$ for all $(x, y) \in \Omega$. This convergence can be visualized in Fig. 24 at the center of the domain. We observe how after $t = 3$, the dynamics of (u, v) are almost entirely driven by those of $(\tilde{u}^*, \tilde{v}^*)$. Thus, as in the ODE level, at the time horizon the spatially homogeneous control $\alpha^*(t)$ effectively reduces the bacterial population considerably.

Without the effect of the control, as Fig. 22 illustrated, the final bacterial population would have nearly achieved $r/(r + a) = 2/3$, its inherent equilibrium, self regulated by the effect of a. However, the use of α^* reduces this value of $u(x, y, t_f)$ to practically $\tilde{u}^*(t_f) \approx 0.137$ for all $(x, y) \in \Omega$. This yields a reduction of approximately 80% on the final bacterial population level with respect to the uncontrolled case.

Therefore, although α^* is possibly not the optimal control for problem (29), as it lacks information regarding the spatial structure of (u, v), as a first approximation to the problem, it offers a feasible solution that is easy to compute and that, at least for this case, yields an acceptable outcome, succeeding in the task of containing the bacterial spread. However, a detailed analytical investigation of problem (29) still has to be carried out in order to assess the quality of this approximation technique.

7. Conclusions

Throughout this work, we numerically investigated the dynamics of system (1) under asymptotically periodic external supplies. Firstly, the numerical experiments carried out in Section 3 allowed us to identify the periodicity threshold for the associated ODE system (3). The results consistently indicate that the sharp threshold $r_{\min}$ that arises for the case $a = 0$ does in fact regulate the periodicity for arbitrary $a > 0$. This is however based only on systematic numerical evidence, and a rigorous analytical proof remains an open problem.

Next, the convergence of the solutions of the PDE system (1) to the solutions of the ODE system (3) and their eventual periodic behavior was tested with different examples by means of the GFD method, with particular interest in the parameter regimes not covered by existing analytical results.

Lastly, an optimal control problem was formulated and an approximate solution was numerically constructed, illustrating how the external supply can be used to prevent species proliferation. As mentioned at the end of Section 6, the obtained solution is based on an heuristic argument, by solving the associated ODE optimal control problem via the Forward-Backward Sweep method. There is however no measure of the optimality of this solution for the PDE optimal control problem. Moreover, such a solution could be constructed solely because we selected a spatially homogeneous control, as otherwise, the ODE reduction would not have been possible. A detailed study of the optimal control problem would help bring light to these aspects.

As a final remark, one of the main advantages of having using the Generalized Finite Difference Method is that it is a meshless technique based solely on scattered nodes. Since the approximation relies on local stars rather than structured grids, the method is intrinsically well suited to irregular boundaries and intricate geometries. In particular, nodes can be distributed along any curved boundary and inside the domain without any modification to the core formulation. The differential operators are locally reconstructed in exactly the same way as for polygonal domains. In addition, the presence of holes or internal boundaries does not alter the method. Each boundary component is treated independently by constructing local stars near the corresponding boundary nodes and enforcing the Neumann conditions there. The ghost-node strategy described in the paper extends naturally to arbitrary geometries. Fictitious nodes are placed along the outward normal direction of each boundary segment (or boundary component), ensuring that the Neumann conditions are imposed consistently regardless of the domain shape. Therefore, no structural change to the

numerical scheme is required, only an appropriate node distribution adapted to the geometry. This flexibility is a well-known strength of GFDM and confirms that the method developed here can be directly applied to circular or multiply-connected computational domains.

CRediT authorship contribution statement

Federico Herrero-Hervás: Writing – review & editing, Writing – original draft, Validation, Software, Methodology, Investigation, Formal analysis, Conceptualization. **Mihaela Negreanu:** Writing – review & editing, Writing – original draft, Validation, Supervision, Project administration, Methodology, Investigation, Funding acquisition, Formal analysis, Conceptualization. **Antonio M. Vargas:** Writing – review & editing, Writing – original draft, Validation, Software, Methodology, Investigation, Formal analysis, Conceptualization.

Declaration of competing interest

The authors declare that they have no known competing financial interests or personal relationships that could have appeared to influence the work reported in this paper.

Acknowledgments

This work was supported by Project PID2022-141114NB-I00 from the Spanish Ministry of Science and Innovation (M.N, A.M.V) and by Grant FPU23/03170 from the Spanish Ministry of Science, Innovation and Universities (F.H.-H.).

Data availability

No data was used for the research described in the article.

References

[1] Herrero-Hervás F, Negreanu M. On a negative chemotaxis system with lethal interaction. Commun Nonlinear Sci Numer Simul 2026;156:109645.
[2] Benov L, Fridovich I. Escherichia coli exhibits negative chemotaxis in gradients of hydrogen peroxide, hypochlorite, and N-chlorotaurine: products of the respiratory burst of phagocytic cells. Proc Natl Acad Sci USA 1996;93(10):4999–5002.
[3] Uhl L, Gerstel A, Chabalier M, Dukan S. Hydrogen peroxide induced cell death: One or two modes of action? Heliyon 2015;1(4).
[4] Seaver LC, Imlay JA. Hydrogen peroxide fluxes and compartmentalization inside growing escherichia coli. J Bacteriol 2001;183(24).
[5] Ravindra Kumar S, Imlay JA. How escherichia coli tolerates profuse hydrogen peroxide formation by a catabolic pathway. J Bacteriol 2013;195(20):4569–79.
[6] Keller EF, Segel LA. Initiation of slime mold aggregation viewed as an instability. J Theoret Biol 1970;26:399–415.
[7] Keller EF, Segel LA. A model for chemotaxis. J Theoret Biol 1971;30:225–34.
[8] Hillen T, Painter KJ. A users guide to PDE models for chemotaxis. J Math Biol 2009;58:183–217.
[9] Horstmann D. From 1970 until present: the Keller–Segel model in chemotaxis and its consequences. Jahresber Dtsch Math-Ver 2003;105(3):103–65.
[10] Bellomo N, Bellouquid A, Tao Y, Winkler M. Toward a mathematical theory of Keller–Segel models of pattern formation in biological tissues. Math Model Methods Appl Sci 2015;25:1663–763.
[11] Herrero-Hervás F, Negreanu M. Asymptotics and periodic dynamics in a negative chemotaxis system with cell lethality. 2025, Preprint. Available at arxiv:2511.06889.
[12] Benito JJ, García A, Gavete L, Negreanu M, Ureña F, Vargas AM. On the numerical solution to a parabolic–elliptic system with chemotactic and periodic terms using generalized finite differences. Eng Anal Bound Elem 2020;113:181–90.
[13] Ureña F, Gavete L, García A, Benito JJ, Vargas AM. Solving second order nonlinear parabolic PDEs using generalized finite difference method (GFDM). J Comput Appl Math 2019;354:221–41.
[14] Herrero-Hervás F, Negreanu M, Vargas AM. Convergence of a meshless numerical method for a chemotaxis system with density-suppressed motility. Comput Math Appl 2023;148:293–301.
[15] Herrero-Hervás F, Negreanu M. Global stability in a negative chemotaxis system with chemically induced lethality. Preprint.
[16] Collatz L. The numerical treatment of differential equations. New York, Heidelberg, Berlin: Springer-Verlag; 1960.
[17] Forsythe GE, Wasow WR. Finite difference methods for partial differential equations. New York: Wiley; 1960.
[18] Jensen PS. Finite difference technique for variable grids. Comput Struct 1972;2:17–29.
[19] Perrone N, Kao R. A general finite difference method for arbitrary meshes. Comput Struct 1975;5:45–58.
[20] Benito JJ, Ureña F, Gavete L. Influence of several factors in the generalized finite difference method. Appl Math Model 2001;25(12).
[21] Lancaster P, Salkauskas K. Curve and surface fitting. Academic Press; 1986.
[22] Vargas AM. Finite difference method for solving fractional differential equations at irregular meshes. Math Comput Simulation 2022;193:204–16.
[23] Liszka T, Orkisz J. The finite difference method at arbitrary irregular grids and its application in applied mechanics. Comput Struct 1980;11:83–95.
[24] Corrêa Vianna Filho AL, Guillén-González F. A review on the analysis and optimal control of chemotaxis-consumption models. SeMA J 2025;82:317–50.
[25] Fleming W, Rishel R W. Deterministic and stochastic optimal control. In: Applications of mathematics series, New York, Heidelberg, Berlin: Springer-Verlag; 1975.
[26] Hackbusch W. A numerical method for solving a parabolic equations with opposite orientations. Computing 1978;20(3):229–40.
[27] Lenhart S, Workman JT. Optimal control applied to biological models. Boca Raton: Chapman & Hall/CRC Press; 2007.
[28] McAsey M, Mou L, Han W. Convergence of the forward–backward sweep method in optimal control. Comput Optim Appl 2012;53:207–26.